Technical Note

Landslides (2023) 20:427–446
DOI 10.1007/s10346-022-01982-9
Received: 29 July 2022
Accepted: 13 October 2022
Published online: 26 October 2022

Matthew E. Cook · Martin S. Brook · Ian J. Hamling · Murry Cave · Jon F. Tunnicliffe · Rachel Holley

Investigating slow-moving shallow soil landslides using Sentinel-1 InSAR data in Gisborne, New Zealand

Abstract Landslides are widespread geomorphological features on the North Island of New Zealand, where they represent one of the primary landscape-forming processes. This study focuses on the steepland terrain surrounding Gisborne, a city located on the east coast of the North Island, at the Hikurangi subduction margin. This terrain consists of young, weak, sedimentary rocks and soils; the most common modes of slope failures are soil creep, slides and flows in shallow, clay-rich soil and regolith, triggered by heavy rainfall. Based on observational data from Sentinel-1 imagery, this study leverages results from interferometric synthetic aperture radar (InSAR) processing to reveal the distribution of deformation across Gisborne's steepland periphery from January 2016 to December 2021. Velocities in the line of sight were obtained from the stack of interferograms and projected along the direction of maximum slope, to extract the true displacement on the slopes. The ascending and descending data sets were combined to reveal the vertical and horizontal components of the deformation. The results were combined with a regional LiDAR data set, aerial imagery and field observations to delineate areas of slope deformation. Finally, slope deformation time series data was compared with rainfall records to identify seasonal changes, due to shrinking and swelling of expansive soils. Although the InSAR displacement data contains some noise, results could be used to identify 132 unstable slopes within the study area, caused by soil creep and earthflows. Also, the shrink-swell of expansive soils causes a seasonal pattern of displacements, which varied by 10–20 mm/year between Austral winter and summer, strongly correlated to rainfall.

Keywords InSAR · Slow-moving landslides · Seasonal deformation · New Zealand · Remote sensing

Introduction

In urban residential areas, landslides are a serious and complex natural hazard that occur in many countries and can have social, economic and environmental impacts (Cruden 1990; Turner 2018). The most common slope failures in New Zealand are slides and flows in shallow soil and regolith triggered by heavy rainfall (Basher 2013; Crozier 2005; Glade 1998; Smith et al. 2021). The scale of erosion ranges from individual landslide events to multiple occurrence landslide events (MORLEs), a particular type of phenomenon that can trigger thousands of landslides on a regional scale (e.g. Crozier 2005). Events of this magnitude make it extremely challenging to map landslides covering such large areas using conventional ground-based mapping practices and site-specific in situ monitoring such as extensometers and inclinometers. Therefore, remote sensing approaches, such as unmanned aerial vehicle (UAV) surveys, light detection and ranging (LiDAR) and interferometric synthetic aperture radar (InSAR), have been used in recent years. These approaches provide complementary data sets to traditional landslide mapping and monitoring techniques to maintain and update landslide inventories (Kromer et al. 2015; Solari et al. 2020) and aid susceptibility analysis (e.g. Smith et al. 2021). In particular, spaceborne SAR imaging systems allow remote areas to be rapidly surveyed without exposing people or equipment to risk, and images can be taken in all weather conditions at night or day, allowing continuous coverage of a site.

Interferometric Synthetic Aperture Radar (InSAR) is an active remote sensing technique used to create DEM and monitor surface deformation on a cm to mm scale accuracy (Hu et al. 2014). Synthetic Aperture Radar imaging systems work by transmitting an electromagnetic pulse from a sensor mounted on an aircraft or satellite to the Earth's surface, and Interferometry exploits the phase difference between two or more SAR images (Ferretti 2014). The standard InSAR technique for mapping ground movement is called differential InSAR (D-InSAR), which uses the repeat pass method to compare two or more SAR images taken over the same area at different times (Simons and Rosen 2007). Over the past three decades, more advanced multi-temporal InSAR (MT-InSAR) techniques have been developed, which use a network of interferograms rather than a single pair to reduce the spatial, temporal and atmospheric decorrelation, enhance the precision of ground deformation, and provide time series analysis (Hu et al. 2014; Osmanoğlu et al. 2016). The algorithms include the Permanent Scatterer InSAR (PS-InSAR; Ferretti et al. 2001; Ferretti 2014) and Small Baseline Subset (SBAS; Berardino et al. 2002; Ferretti 2014; Lanari et al. 2004; Yunjun et al. 2019) methods, and approaches which combine the two (Hu et al. 2014; Osmanoğlu et al. 2016) such as the Stanford Method for Persistent Scatterers (StaMPS; Hooper 2008) and SqueeSARTM (Ferretti et al. 2011). The method depends on the data available, the study area and the information the user is trying to extract. The PS-InSAR method typically uses a single SAR image, called the reference, from which all interferograms are formed and uses radar targets considered coherent over time, called point scatterers (PS), such as buildings (Ferretti 2014). For this reason, the method is better suited for urban environments containing more coherent targets. The SBAS technique is more appropriate in rural areas, as the approach uses pixels that are spatially coherent in the interferograms called distributed scatterers (DS; Ferretti 2014). The SBAS method produces a network of interferograms with short temporal intervals and spatial baselines to increase

interferogram correlation instead of having one reference image (Hooper 2008; Yunjun et al. 2019). In this study, we adopted an SBAS-based method for our InSAR time series analysis.

A wide range of data is available from current and previous SAR satellite missions, and different levels of resolution and spatial and temporal coverage can be acquired, depending on project requirement (Wasowski and Bovenga 2014). The maximum velocity detectable by a SAR satellite is constrained by its temporal resolution (revisit time), spatial resolution and the angle of the land surface (Wasowski and Bovenga 2014). For Sentinel-1, the spatial resolution is approximately 5 m (E-W) by 20 m (N-S). With a revisit time of 12 to 24 days in New Zealand such monitoring is particularly well suited to very slow- (16 mm/year to < 1.6 m/year) or extremely slow- (< 16 mm/year) moving landslides (c.f. Hungr et al. 2014; Notti et al. 2014; Colesanti and Wasowski 2006; Wasowski and Bovenga 2014). The application of InSAR to map and monitor slow-moving deformation related to landslides is well documented globally (Aslan et al. 2020; Béjar-Pizarro et al. 2017; Barra et al. 2016; Colesanti and Wasowski 2006; Crosetto et al. 2018; Del Soldato et al. 2019; Isya et al. 2019; Notti et al. 2014; Wasowski and Bovenga 2014; Xue et al. 2021). However, the application of InSAR for geotechnical purposes in New Zealand is in its infancy, even though the technique has been used successfully to investigate other natural hazards such as volcanoes (Hole et al. 2007; Hamling et al. 2015; Hamling 2020; Harvey 2021) and earthquakes (Barnhart et al. 2011; Atzori et al. 2012; Elliott et al. 2012; Hu et al. 2012; Liu et al. 2022).

This study focuses on terrain surrounding Gisborne, a city located on the East Coast of New Zealand's North Island (Fig. 1). The region is characterised by steep slopes and narrow ridgelines, and the primary type of landslides are flows and slides in shallow soils, triggered by heavy rainfall. Previous studies have attempted to delineate landslide hazards in Gisborne (Mazengarb 1997) and have mapped a number of landslide locations (Fig. 1). However, the work did not identify areas at risk with any precision, and current landslide inventories are often only related to individual residential properties and the failure of retaining walls, in particular. Indeed, the extent and ongoing surface deformation of landslides in the Gisborne area are poorly known, and areas at risk from slope instability are often unknown until a slope failure occurs. For example, slope failures have been active at several residential properties in the city (Davies and Cave 2017; Cook et al. 2022), where buildings and infrastructure are still at risk from further deformation caused by slow-moving, complex landslides. Also, limited space on the low-lying flood plain means that there is growing incentive to build residential housing on increasingly precarious terrain on slopes surrounding the city. Potentially, property damage can be prevented if precursory information on slow deformation is available and incorporated into planning and engineering interventions. In this study, Sentinel-1 InSAR data is used to identify slopes undergoing active ground deformation, and these results are combined with airborne LiDAR data and aerial imagery to map areas of deformation. Analysis of InSAR-generated displacement time series provides good insight into the timescales and magnitude of slope movement, identifies potential periods of acceleration or quiescence in particular areas, and links the intra-annual deformation with seasonal rainfall patterns.

Study area

Geology

Gisborne (Fig. 1) is primarily built upon the Poverty Bay Flats, a low-lying alluvial flood plain of the Waipaoa River. Surrounding the plains are steep hills, not exceeding 800 m above sea level, well-known for high erosion rates because of the soft, young sedimentary rocks and soils, and the lack of vegetation cover due deforestation and overgrazing (Basher 2013; Franks 1988). The drainage in the area consists of a number of incised valleys and gullies, tributaries of the Waimata River. The geology and geomorphology of Gisborne is strongly controlled by the region's location in the forearc of the Hikurangi subduction margin (Lacoste et al. 2009). The Pacific plate is subducting beneath the Australian plate at ~ 50 mm/year, subjecting the area to uplift rates of ~ 2 mm/year (Lacoste et al. 2009). The geology of Gisborne consists of weak sediments and is shown in Fig. 1c. The Early Cretaceous to Early Miocene fault-bounded "melange" rocks were emplaced in the late Miocene. These consist of complex, sheared, smectite-rich mudstones (Mazengarb 1997; Speden 2004). The Miocene-Pliocene bedrock of the Tolaga Group and Mangaheia Group are the primary lithofacies in the area (Fig. 1c), and dip angles range between vertical and horizontal, but are primarily < 30° (Mazengarb 1997). The Tolaga Group consists of carboniferous turbidites and calcareous sandstones and siltstones. The Pleistocene Mangatuna Formation contains gravels, tephra-rich sands, siltstones and smectite clays (Mazengarb 1997). No active faults in the Gisborne area have been mapped, although there is the possibility that faults could be buried beneath younger sediment, that may be reactivated in future (Mazengarb 1997; Speden 2004).

Landslide hazards

Slope instability in Gisborne is controlled by several factors, including steep slopes, relatively young, soft geology, reactivation of previous failures, discontinuity orientation, deforestation, the undercutting of slopes and high erosion rates (Basher 2013; Crozier 2010; Glade 2003; Phillips et al. 2018; Mazengarb 1997). Many of the hills around Gisborne currently display a terracette (stepped) morphology, caused by soil creep on steep slopes facilitated by shrinking and swelling of soils and overgrazing by animals (Hungr et al. 2014; Vincent and Clarke 1980). Records of previous events (citation—even pers. comm.) reveal several sites of slope instability across the steep slopes of the peri-urban area, and along riverbanks and terraces (Fig. 1). The majority of recorded landslides in Gisborne occur in shallow soil, but there is evidence of deep-seated landslides occurring in Gisborne city (Mazengarb 1997). Across the urban area, shallow landslides frequently occur along reactivated slip surfaces in the highly-weathered Pleistocene Mangatuna Formation, particularly in the Mangapapa, Whataupoko and Kaiti suburbs (Fig. 1b). The formation comprises alluvial gravels, tephra-rich sands and high plasticity montmorillonite and bentonite (Mazengarb 1997). Previously identified landslides include rotational slumps and earthflows (Cook et al. 2022; Davies and Cave 2017), and some failures have been known to occur on slopes with angles as low as 5° (Mazengarb 1997). Shallow soil failures are also common within the regolith overlying the Miocene and Pliocene bedrock in the east of the study area in Wainui, Okitu and Makorori (Fig. 1). Despite the

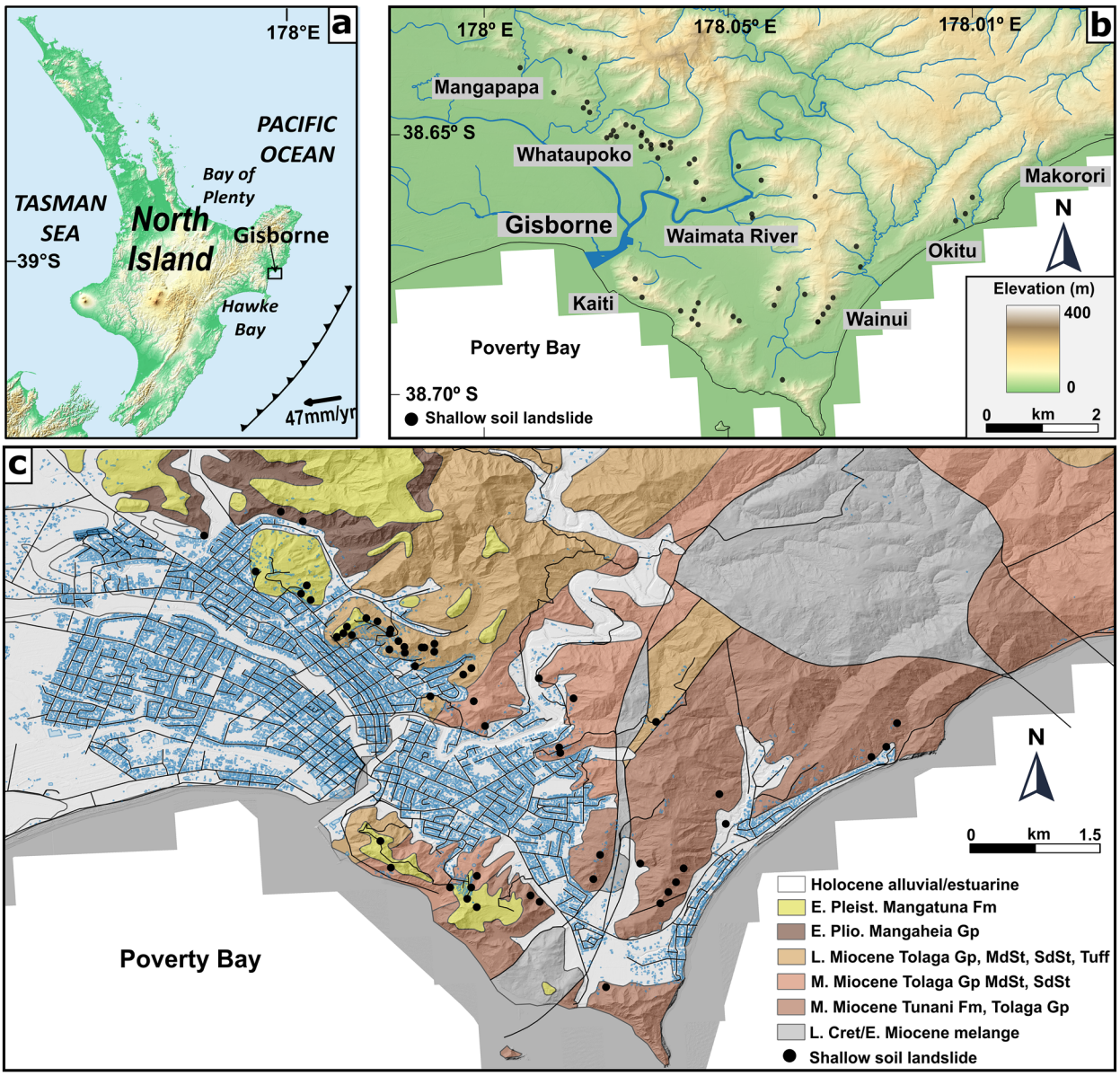

Fig. 1 **a** Location of Gisborne on the North Island in relation to the major structures of the convergent Hikurangi margin; **b** elevation map of Gisborne City, with historic shallow soil landslide locations; **c** map of the primary lithologies in the study area, landslide locations and property outlines are represented by blue polygons

location close to the Pacific-Australian plate boundary, the primary trigger of landslides in Gisborne is extreme rainfall events. Over the last few decades, these have included ex-tropical cyclone Bola in 1988 (Franks 1988), the Labour Weekend storm in 2005 (Beetham and Grant 2006), ex-tropical cyclones Debbie and Cook in 2017 (Cook et al. 2022), and a slow-moving tropical storm in November 2021. Examples of landslides occurring after the November 2021 storm are displayed in Fig. 2. These extreme storm events can trigger multiple landslides on slopes (Crozier 2005), particularly on bare slopes lacking vegetation that have been undercut by rivers, roads and farm tracks (Fig. 2). Within the developed residential areas, inappropriate slope engineering on already unstable slopes contributes to instability and failure of retaining walls (e.g. Fig. 2g).

Methods

Data and processing

This study used Sentinel-1 single look complex images from the interferometric wide-swath mode acquired from January 2016 to December 2021 for descending and ascending orbit directions. Information regarding the Sentinel-1 data sets used in this study is presented in Table 1. From the descending track 175, 137 acquisitions were used to generate a stack of 409 interferograms and 163 images were used from the ascending track 8 to generate a stack of 487 interferograms. The network of interferograms used in this study for ascending and descending is shown in Fig. 3. Three connections per image were used to reduce the temporal decorrelation, particularly between seasons

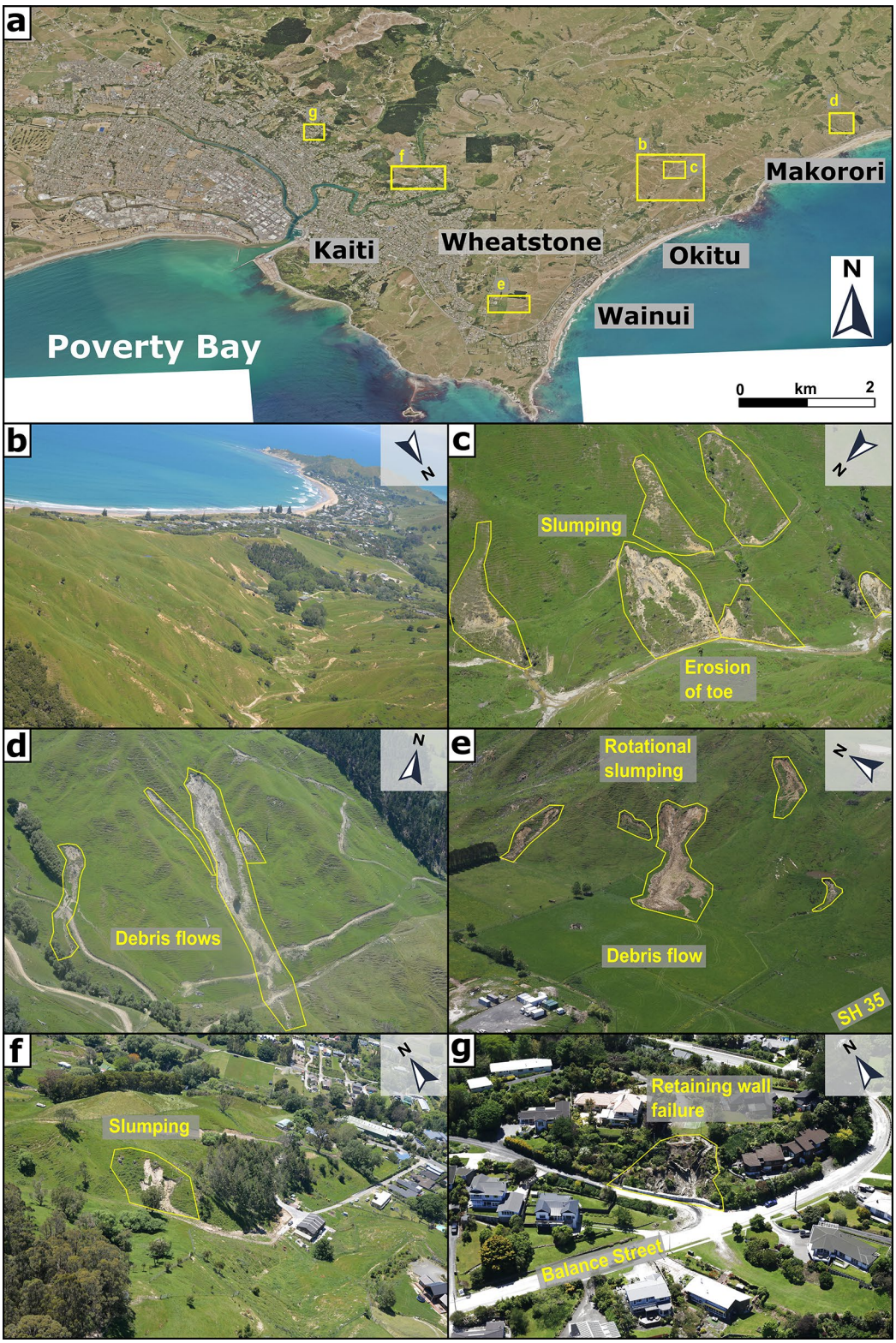

Fig. 2 **a** Shallow soil landslide locations across Gisborne City; **b** multiple individual failures occurring across slopes; **c**, **d**, **e**, **f** shallow soil slumping and earthflows are occurring on steep bare slopes undercut by streams, farm tracks and roads; **g** example of an unconsented retaining wall failure

Table 1 Details of the Sentinle-1 SAR images used to generate interferograms (Intf.) and the number of coherent points identified in the V_{LOS} (Fig. 5) and V_{SLOPE} (Fig. 6)

Satellite	Orbit geometry	Track No.	Sub-swath	No. of acquisitions	No. of Intf	Acquisition period	V_{LOS} points	V_{SLOPE} points
S1A/S1B	Descending	175	1	137	409	2016–2021	59,606	24,853
S1A/S1B	Ascending	8	2	163	487	2016–2021	72,632	26,887

(Fig. 3c), although several longer temporal baselines are included to reduce the effects of fading signals and improve detection of long-term deformation (e.g. De Luca et al. 2022). The acquisitions used for the long temporal baselines were selected from the winter months, which have higher average coherence (Fig. 3c). In order to maintain a higher spatial resolution and help detect smaller landslides (< 50 m²?), a low number of multi-looks were selected, with 5 and 1 in range and azimuth direction, respectively. The Sentinel-1 images were processed using ISCE (Rosen et al. 2012), and displacement and time series were obtained using MintPY (Yunjun et al. 2019). We applied the small baseline subset (SBAS) technique (Berardino et al. 2002; Li et al. 2022) to identify landslide-related deformation within the study area. All measurements were taken with respect to a stable reference point within the study area that was assumed to be nondeforming (38.664 S, 178.020 E).

VSLOPE calculations

The relationship between the geometry of the slope and the sensor is extremely important when using InSAR to map landslides. This is because the actual displacement of a slope can only be obtained if the dip direction of the slope is parallel to the line of sight (LOS) of the sensor (Colesanti and Wasowski 2006; Notti et al. 2014), which is generally in an approximately eastward (ascending) or westward (descending) direction. For most landslides, deformation commonly occurs in the direction of the steepest slope, particularly translational landslides (e.g. Hungr et al. 2014). Thus, a standard method used to identify the actual component of the landslide movement is to project the LOS velocity (V_{LOS}) along the direction of the slope (V_{SLOPE}) (Notti et al. 2014). The V_{SLOPE} is obtained using:

$$V_{SLOPE} = \frac{V_{LOS}}{C} \tag{1}$$

where C is the coefficient derived from the LOS and downslope vectors in the north, east and upward directions. Certain slopes will produce points with a low C value, close to 0, which will exaggerate the V_{SLOPE}. This low sensitivity is caused by noisy V_{LOS} data or unfavourable slope orientation, such as north or south-facing slopes, which are perpendicular to the sensor's LOS. In order to avoid anomalous V_{SLOPE} values, points with $-0.2 < C < 0.2$ are removed, as proposed by Notti et al. (2014). Also, positive V_{SLOPE} values are removed as they would represent uphill movement on slopes. The coefficient is calculated using the following equation:

$$C = (E \times E_{SLOPE}) + (N \times N_{SLOPE}) + (U \times U_{SLOPE}) \tag{2}$$

The LOS vectors are a component of the incidence angle (α) and heading angle (γ) of the sensor in radians, and the downslope vectors are calculated from the slope (s) and aspect (a) (Notti et al. 2014), which are derived from a 10 m by 10 m 2019 digital elevation model (DEM):

LOS vectors:

$$E = -1 \times \sin(\alpha) \times \sin(\gamma) - \frac{3 \times \pi}{2} \tag{3}$$

$$N = -1 \bullet \sin(\alpha) \bullet \cos(\gamma) - \frac{3 \times \pi}{2} \tag{4}$$

$$U = \cos(\alpha) \tag{5}$$

Downslope vectors:

$$E_{SLOPE} = -1 \times \cos(s) \times \sin(a - 90) \tag{6}$$

$$N_{SLOPE} = \cos(s) \times \sin(a - 90) \tag{7}$$

$$U_{SLOPE} = \sin(s) \tag{8}$$

Vertical and horizontal calculations

Determining slope deformation is more challenging for specific slopes, such as those in a north–south direction (1). However, with data sets from two different viewing geometries, the vertical and horizontal (E-W) movement can be obtained by combining the LOS vectors in the eastward (E) and upward (U) directions, and the velocity in the direction of LOS (V_{LOS}) for the ascending (V_{asc}) and descending (V_{desc}) data sets (Notti et al. 2014). Only neighbouring SBAS points from the ascending and descending data sets which are within 5 m of each other are used for the analysis, using the following formula:

$$V_{EW} = \frac{\left(\left(\frac{V_{desc}}{U_{desc}}\right) - \left(\frac{V_{asc}}{U_{asc}}\right)\right)}{\left(\left(\frac{E_{desc}}{U_{desc}}\right) - \left(\frac{E_{asc}}{U_{asc}}\right)\right)} \tag{9}$$

$$V_{VERT} = \frac{\left(\left(\frac{V_{desc}}{E_{desc}}\right) - \left(\frac{V_{asc}}{E_{asc}}\right)\right)}{\left(\left(\frac{U_{desc}}{E_{desc}}\right) - \left(\frac{U_{asc}}{E_{asc}}\right)\right)} \tag{10}$$

Identifying unstable slopes

In order to identify deforming slopes in the study area, several thresholds were used to ensure the most reliable SBAS points were used, and that the velocity measurements are the best representation of slope deformation. Thus, the deformation along the slope direction (V_{SLOPE}) was used instead of the velocity in the LOS (V_{LOS}) to provide a more reliable indication of slope deformation. The process of identifying unstable slopes is outlined in Fig. 4 using

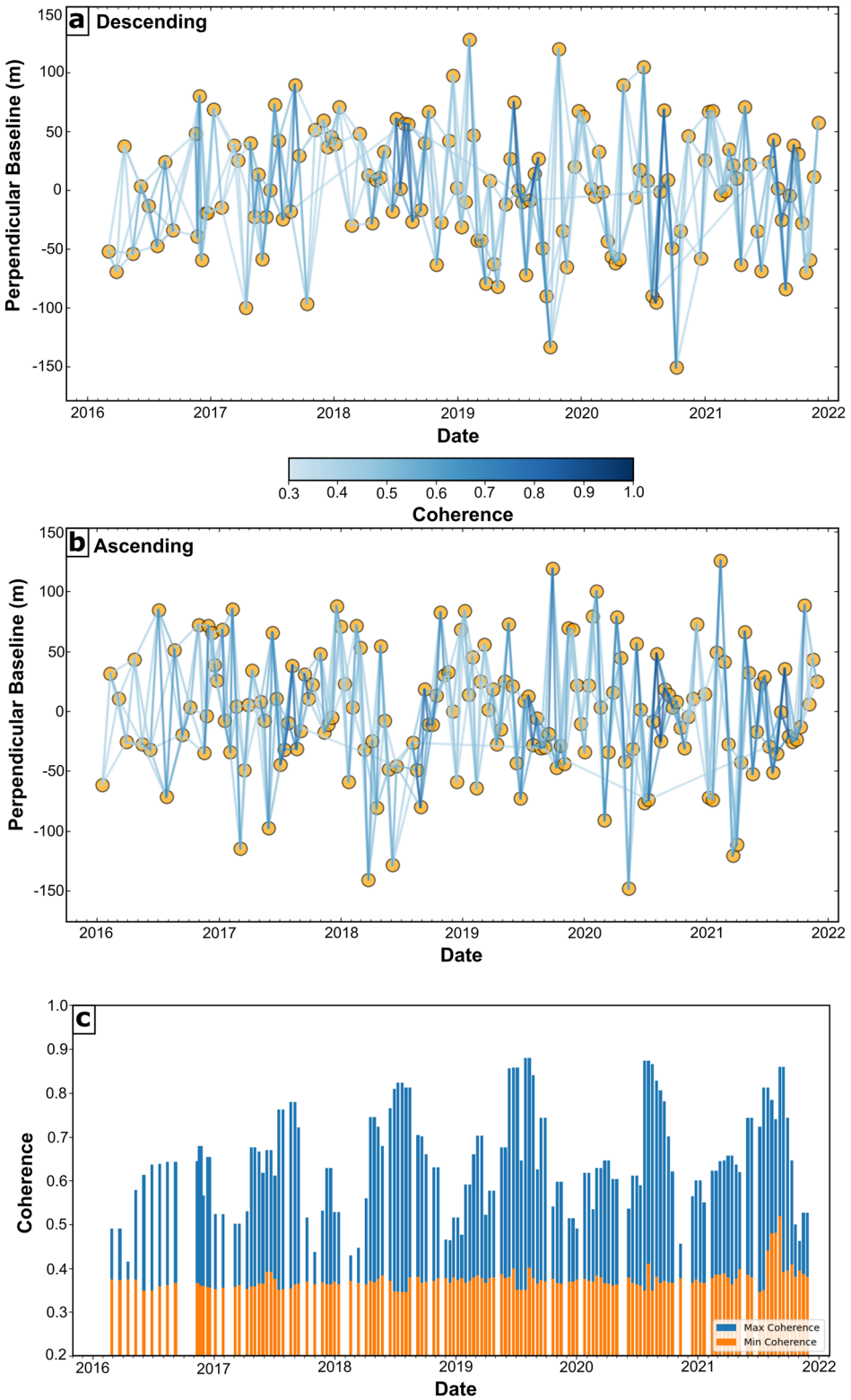

Fig. 3 **a** Network of interferograms with three connections per SAR image and longer temporal baselines selected in the winter months from the descending data set; **b** network of interferograms from ascending data set; **c** coherence plot of the SAR images showing high coherence peaks in the winter months

an example of slopes north of Okitu (see location in Fig. 2a and b). First, the V_{LOS} (Fig. 4a) was converted into the V_{SLOPE} (Fig. 4b) using Eq. 1, and a threshold for the minimum slope angle was set at 5°, which is thought to be the lowest plausible angle for landsliding in the study area (Mazengarb 1997). Then, deforming slopes were defined by having clusters of 5 or more points with downslope V_{SLOPE} values larger than − 10 mm/year (Fig. 4c). This threshold is based on work by Mansour et al. (2010), who associated potential for 'moderate damage to buildings and infrastructure' with displacement rates between − 10 and − 100 mm/year (Mansour et al.

2010). The InSAR deformation results were overlaid on a LiDAR hillshade acquired in 2019 and aerial imagery to define polygons representing the extent of deforming areas and identify deformational structures (Fig. 4d and e). Also, areas of deformation that were not related to unstable slopes, such as stripping and regrowth of vegetation, ploughing of crop fields and construction/excavations, were excluded. Site photos are also used to help ground-truth the areas of instability (Fig. 4f).

Results

InSAR displacement rates

The mean LOS velocity results obtained from both ascending and descending data sets are displayed in Fig. 5. For each data set, movement away from the satellite is represented by negative values (red) and movement towards the satellite is represented by positive values (blue). Values of the V_{LOS} range between − 20 mm/year and 20 mm/year, and the majority of the deformation in both viewing geometries is away from the sensor (Fig. 5). As expected, the point density is greater in the urban area due to the high abundance of coherent targets, such as buildings and roads. Fewer points were detected on the slopes north of the urban area, which is likely due to a large number of pine trees on the slopes (Fig. 2a), compared to the slopes east of the urban area, which are vegetation-free and the soil is exposed (Fig. 2a). A higher-density cluster of coherent points was detected from the ascending data set (72,632) than the descending (59,606), which is attributed to the favourable orientation of the slopes in the study area to the ascending sensor. The V_{SLOPE} values are displayed in Fig. 6, and the maximum downslope movement detected is − 69 mm/year from the descending data set and − 79 mm/year from the ascending data. Areas displaying the highest deformation rates along the V_{LOS} and V_{SLOPE} occur on the slopes north of

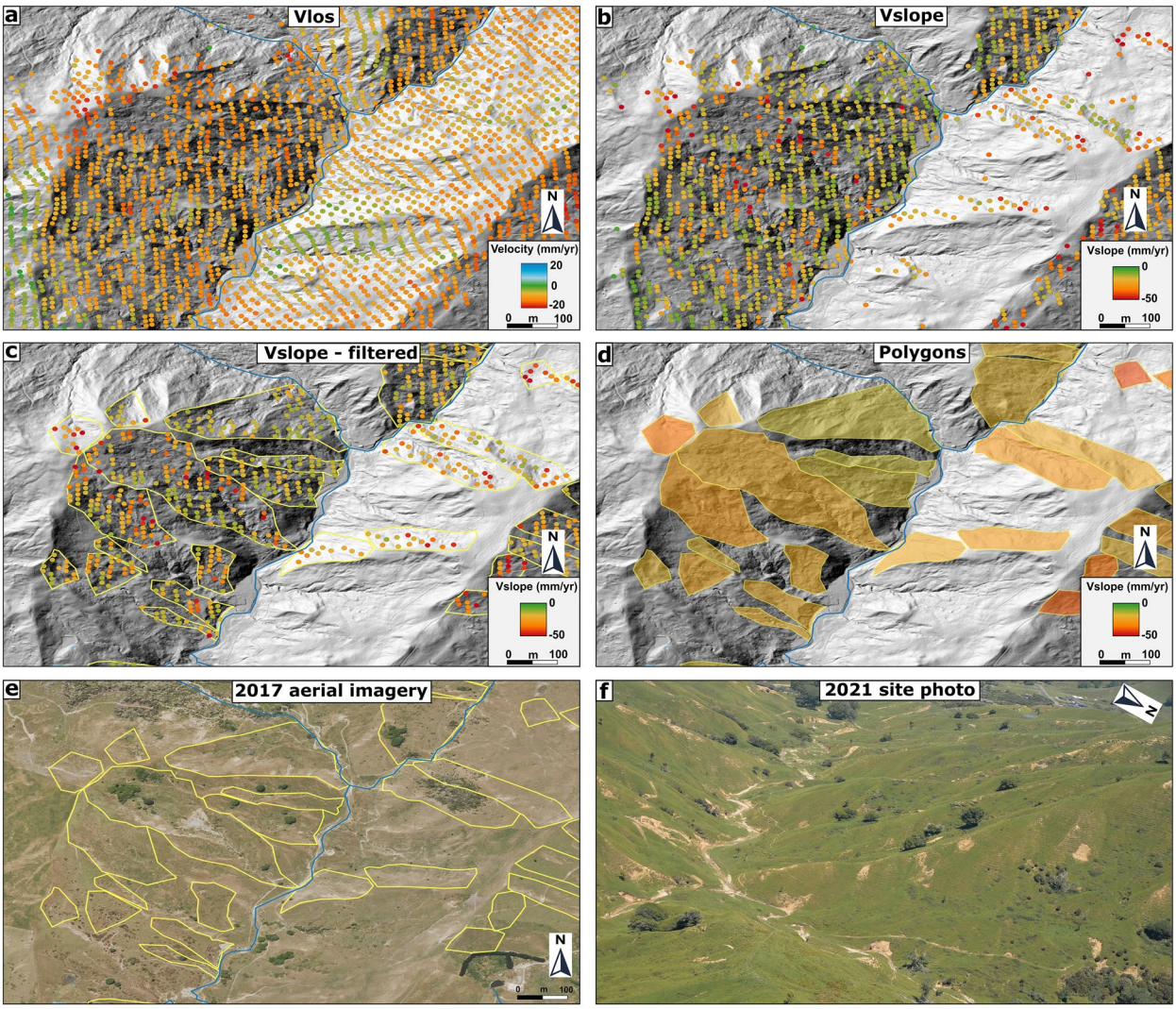

Fig. 4 **a** The VLOS map; **b** V_{SLOPE} map; **c** V_{SLOPE} map filtered to only identify deforming points on slopes and polygons based on a collection of points on a slope and the slope morphology derived from the hillshade and aerial imagery; **d** average V_{SLOPE} of the polygons; **e** aerial imagery used to help identify unstable slopes; **f** site photos following the November 2021 storm

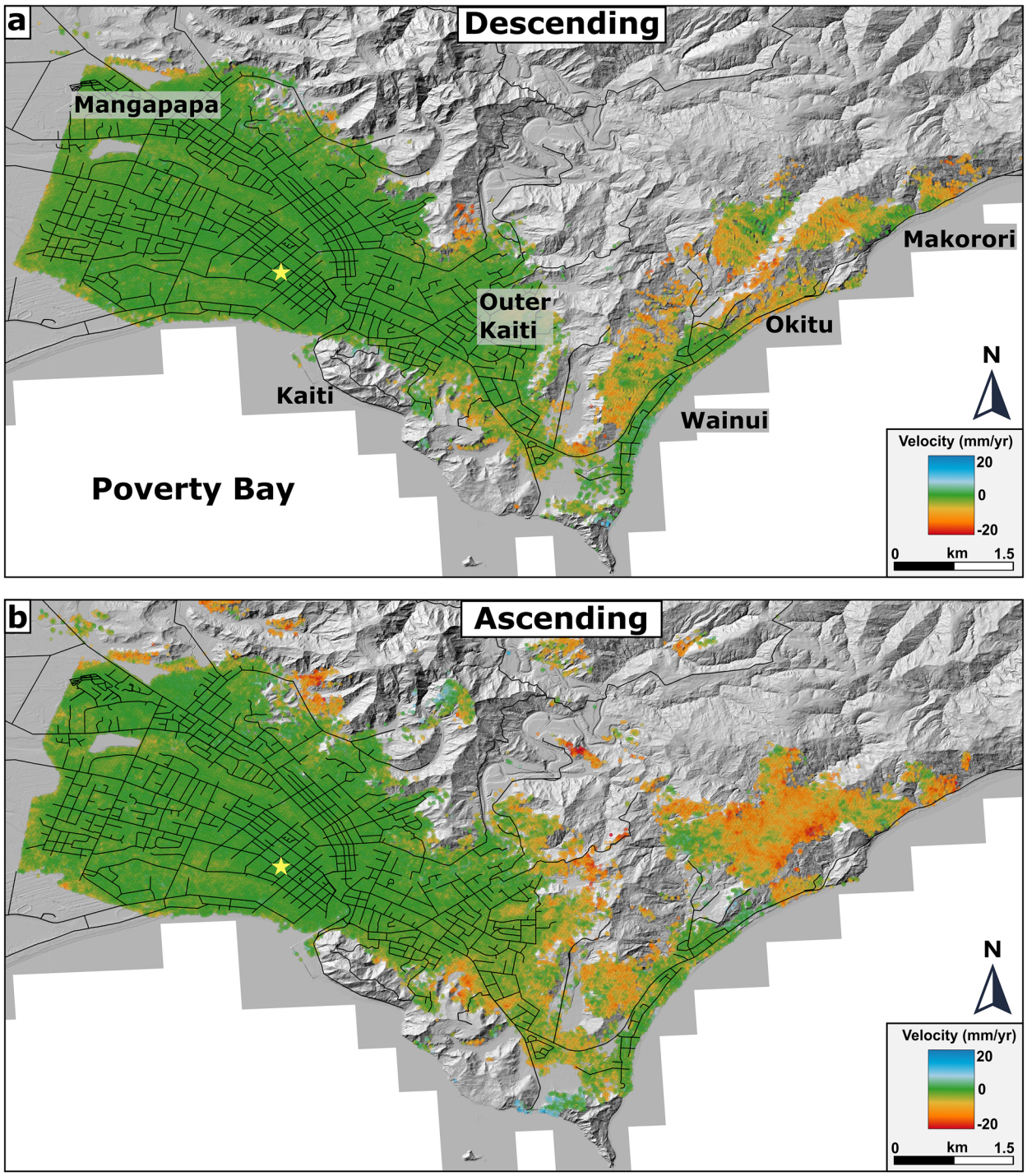

Fig. 5 **a** Map of the mean velocity in the direction of the line of sight (observation period 2016–2021) from the descending orbit track 175 over Gisborne City. The yellow star represents the stable reference point, and negative values (red) indicate movement away from the satellite, and positive values (blue) represent movement towards the satellite; **b** mean LOS velocity map from the ascending orbit track 8 (Observation period 2016–2021)

Mangapapa, the slopes surrounding Outer Kaiti, on Wainui's east-facing slopes and the steep slopes east of the city between Okitu and Makorori (Figs. 5 and 6). In contrast, the low-lying urban areas are unaffected by substantial deformation (Figs. 5 and 6).

The results of the E-W and vertical components are presented in Fig. 7. The maximum deformation in the eastward component (positive values) is 18 mm/year and − 15 mm/year in the westward direction (negative values). Movement along slopes in the EW

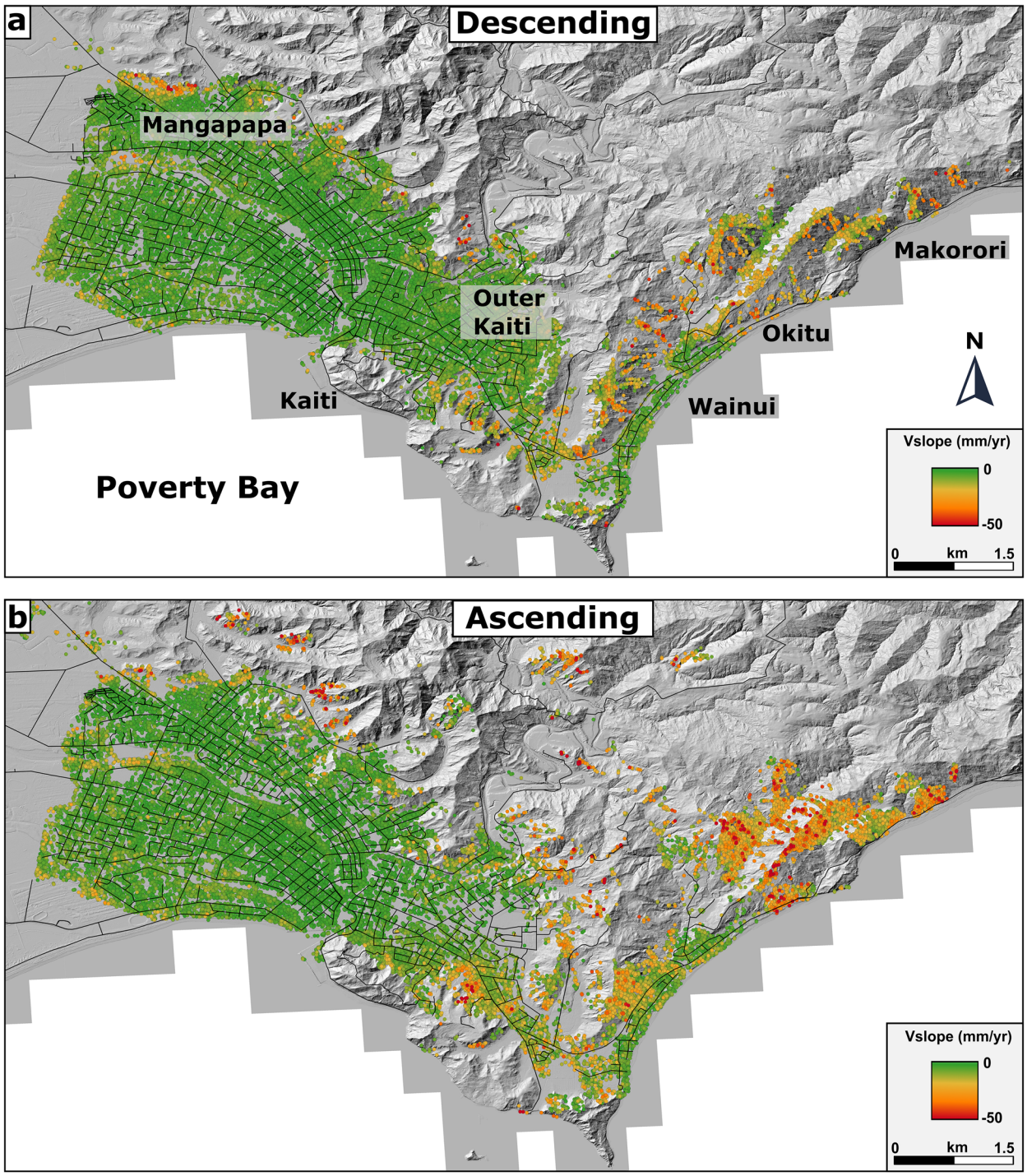

Fig. 6 **a** Map of the velocity projected in the direction of maximum slope (V_{SLOPE}) over Gisborne City from the descending orbit track. Negative values (red) indicate movement downslope, and positive values, which represent movement uphill, have been removed; **b** V_{SLOPE} map from the ascending orbit track

component is associated with translational deformation. Across the study area the movement in an eastward direction is more prominent, particularly on the east-facing slopes surrounding Okitu and Makorori. This aligns with the pattern of values obtained in the V_{LOS} and V_{SLOPE} analysis, indicating that material on this slope is moving downslope. Vertical deformation rates show a strong downward component (negative) across the study area, with values reaching up to − 19 mm/year. The high vertical components are associated with ridgelines on the east-facing slopes in Wainui, and on the slopes between Okitu and Makorori, consistent with likely dominant vertical motion within headscarps and rotational slumping locations (e.g. Fig. 2).

Areas of deformation and displacement time series

In total, 132 sites showed evidence of deformation during the observation period; these are displayed in Fig. 8, with characteristics of the data set in Table 2. The polygons are assigned a value based on the average V_{SLOPE} velocity of all points within the polygon. The average V_{SLOPE} velocity of the deforming slopes is 20 mm/year in the downslope direction. Comparing the data set with the E-W and vertical components, the slopes displayed deformation most predominantly in the downward and eastward directions (Fig. 7). This

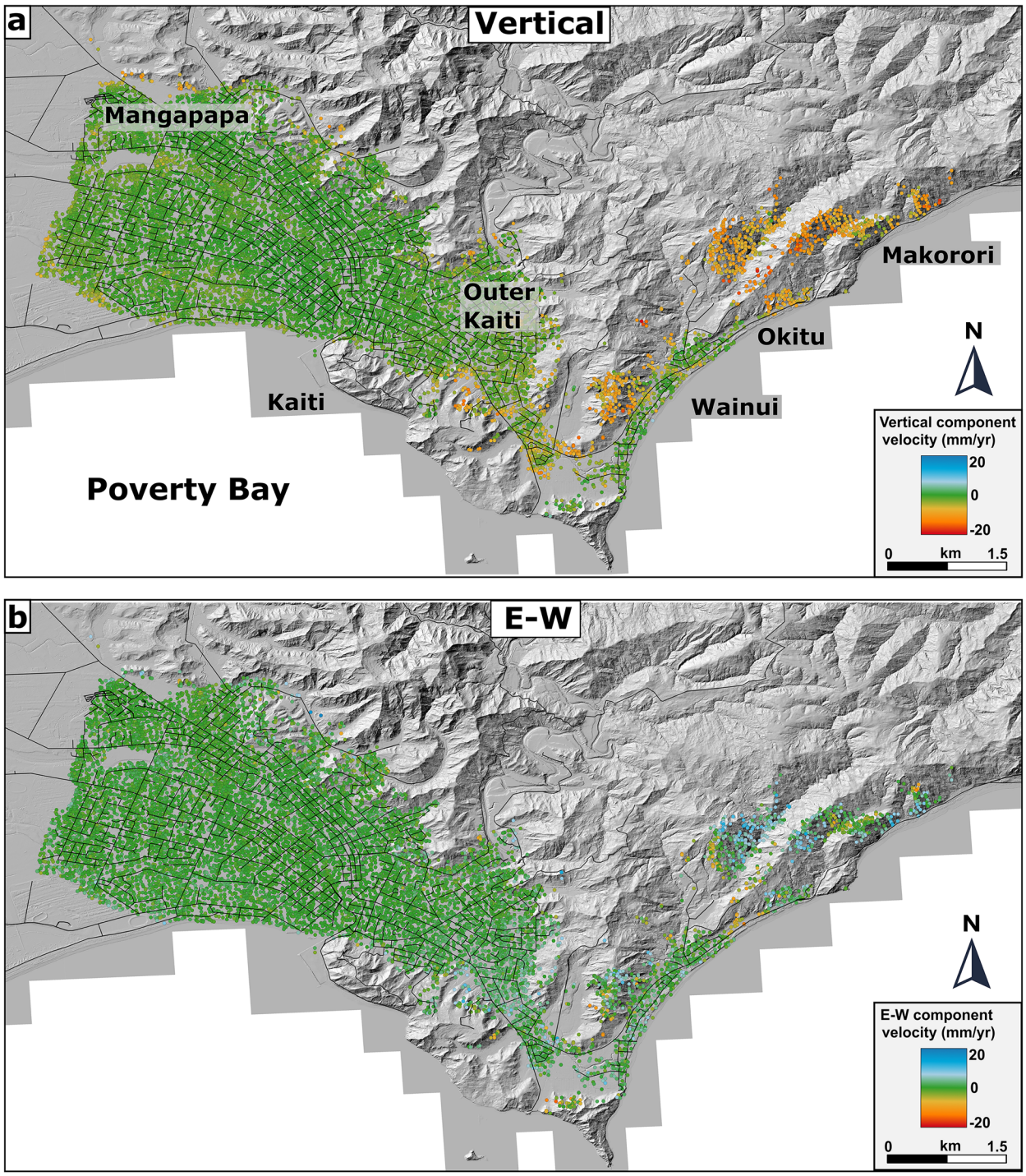

Fig. 7 **a** Velocity map projected in the vertical direction over Gisborne City by combining the descending and ascending viewing geometries. Negative values (red) indicate movement downslope, and positive values (blue) represent uplift; **b** velocity map projected in the horizontal (E-W) direction over Gisborne City by combining the descending and ascending viewing geometries. Negative values (red) indicate movement westward, and positive values (blue) represent movement in an eastward direction

is in accordance with the ascending and descending V_{LOS} values (Fig. 5). The majority of unstable areas were identified with V_{SLOPE} points from the ascending data set (106) and are on slopes with an average orientation of 151° (SSE) and a slope angle of 23°. From the descending data set, 38 points were identified on slopes with an average orientation of 200° (SSW) and slope angle of 23° (Fig. 8). The unstable areas are primarily on the large steep slopes to the east of the urban area (Fig. 8), and some are in the vicinity of critical infrastructures such as State Highway (SH) 35 and residential dwellings. Many of the deforming slopes identified with the InSAR show signs of previous or active instability, such as soil creep and rotational slumping, in the aerial and hillshade imagery (Figs. 9 and 10). However, some of the long-term, slow-moving creep displacement identified using InSAR is not yet visible in the imagery. This implies that the InSAR results are identifying previously unrecognised areas of ongoing deformation that may accelerate during heavy rainfall events. Deformation occurred on slopes within all the major lithofacies present in the area, although most occurred on the steep, east to southeast-facing slopes of the Mid-Miocene Tunanui Formation of the Tolaga Group mudstone (Fig. 1). The Tunanui Formation is present in the east of the study area and outcrops are exposed along the coast between Wainui and Makorori (Fig. 1), where the beds dip—unfavourably—towards the coast.

Three zones affected by deformation were selected to highlight the impacts of slope instability in the study area, and their locations are displayed in Fig. 8b. Zone 1 contains the southeast-facing slopes located in the northeast of the study area at Makorori adjacent to SH35 (Fig. 9). The slopes have an average dip angle of 24°. Underlying the surface soil are interbedded mudstones and sandstones of the Tunanui Formation, which have a bedding dip angle of 54° to the southeast. In the 2017 aerial image, exposed and eroded material is visible on the slopes, ridgelines and gullies (Fig. 9b). The results from V_{SLOPE} analysis could be used to help define the extent of the deformation on the slopes, with average downslope deformation of 24 mm/year, and maximum values reaching 75 mm/year (Fig. 9). The highest deformation values are observed at the head of the gullies or below local scarps. Following a string of ex-tropical storms in November 2021, sections of the slope became affected by several failures, and these were characterised by slumping that transitioned into earthflows, constrained within narrow gullies (Fig. 9c). The earthflows were too rapid to be measured by InSAR. However, the results from the V_{SLOPE} analysis could be used to help define the extent of the deformation in areas displaying evidence of soil creep and deformation, particularly at the top of the gully which transitioned into the earthflow (Fig. 9a).

Zone 2 is located on an eastward facing slope between Okitu and Makorori (Fig. 8b), and several unstable slopes were delineated in the area. The slopes have an average dip angle of 24°, and historic scarps and hummocky ground can be observed in the hillshade map (Fig. 10a). The slopes are vegetation-free and are undercut by a river and several farm tracks along the slope (Fig. 10b). Exposed sediment can be seen along the narrow gullies and surrounding the dirt tracks, indicating active deformation is occurring on the slopes (Fig. 10b). The highest V_{SLOPE} values in the area are 60 mm/year downslope, and these occur near the ridgelines and in narrow gullies along the slope (Fig. 10). A point was selected from one of the polygons (P1) to evaluate the time series of deformation in the LOS, compared to monthly precipitation patterns (Fig. 10c). The deformation in the LOS time series shows that since 2016 there has been a continuous movement away from the sensor downslope, with deformation rates accelerating in 2017 to − 20 mm/year. In comparison, at zone 3, which is located on the east-dipping slopes above Wainui (Fig. 12), the LOS deformation time series of P2 shows a strong seasonal component (Fig. 12c). Peaks in the deformation occur during the winter months (June–August), which can be attributed to the shrinkage of the clay soils in the dry summer months and swelling during the wet winter months. However, the overall trend indicates P2 is moving away from the sensor in a downslope direction. The average V_{SLOPE} in the area is − 15 mm/year, and the maximum V_{SLOPE} in the area reaches up to − 49 mm/year. The hillshade shows multiple relict headscarps below the ridgeline, several scarplets are exposed further downslope, and exposed sediment can be seen in the aerial imagery, most likely caused by soil creep (Fig. 12). Understanding the deformation rates and patterns in zone 3 is of particular interest as it is situated in an area of multiple residential properties under development along the ridgeline.

Discussion

Coverage and landslide mapping

In the context of our investigations in the Gisborne area, InSAR analysis has led to the identification of areas of deformation on slopes in developed and emerging peri-urban zones. Combined with the LiDAR data set, high-resolution aerial imagery and site photos, the InSAR results have proven exceptionally useful for generating objective boundaries of potential landslide sites. Some of these exhibit signs of active slumping and flows, while others show high levels of soil creep and the potential for future instabilities. The coherent points on slopes were primarily located on west to southwest and east to southeast-orientated slopes with a slope angle < 50°. This is in accordance with what can typically be detected by Sentinel-1, due to the layover and shadowing effects (Aslan et al. 2020; Van Natijne et al. 2022). The deformation detected on most of the slopes in Gisborne displays a strong signal in the downslope direction (Fig. 6), with evidence of vertical and translational (E-W) movement. Vertical deformation signals are more prominent than those arising from the translational deformation along the slopes (Fig. 7; e.g. Schlögel et al. 2015). This dominant vertical signal is perhaps attributable to subsidence and slumping of multiple retrogressive scarps in the area. Indeed, when mapping landslides with InSAR, the geometry of the slope and type of failure are essential factors to consider when choosing how to project the velocity and how the surface deformation is interpreted (Notti et al. 2014; Schlögel et al. 2015). For example, the V_{LOS} and V_{SLOPE} values are most effective when detecting slope movement parallel to the LOS of the sensor, such as translational slides (Bianchini et al. 2013; Colesanti and Wasowski 2006; Wasowski and Bovenga 2014; Notti et al. 2014). By contrast, rotational landslides generally exhibit some vertical movement at the headscarp, which can be detected by combining two viewing geometries, allowing the vertical and horizontal (EW) components to be extracted. Multiple measurements in different directions are beneficial, as different parts of the landslide may undergo different rates and directions of movement (Glastonbury and Fell 2008; Schlögel et al. 2015). This was apparent in Gisborne, where most landslides are complex, involving soil creep and rotational slumping, which transition into translational earthflows or mudflows (Fig. 2).

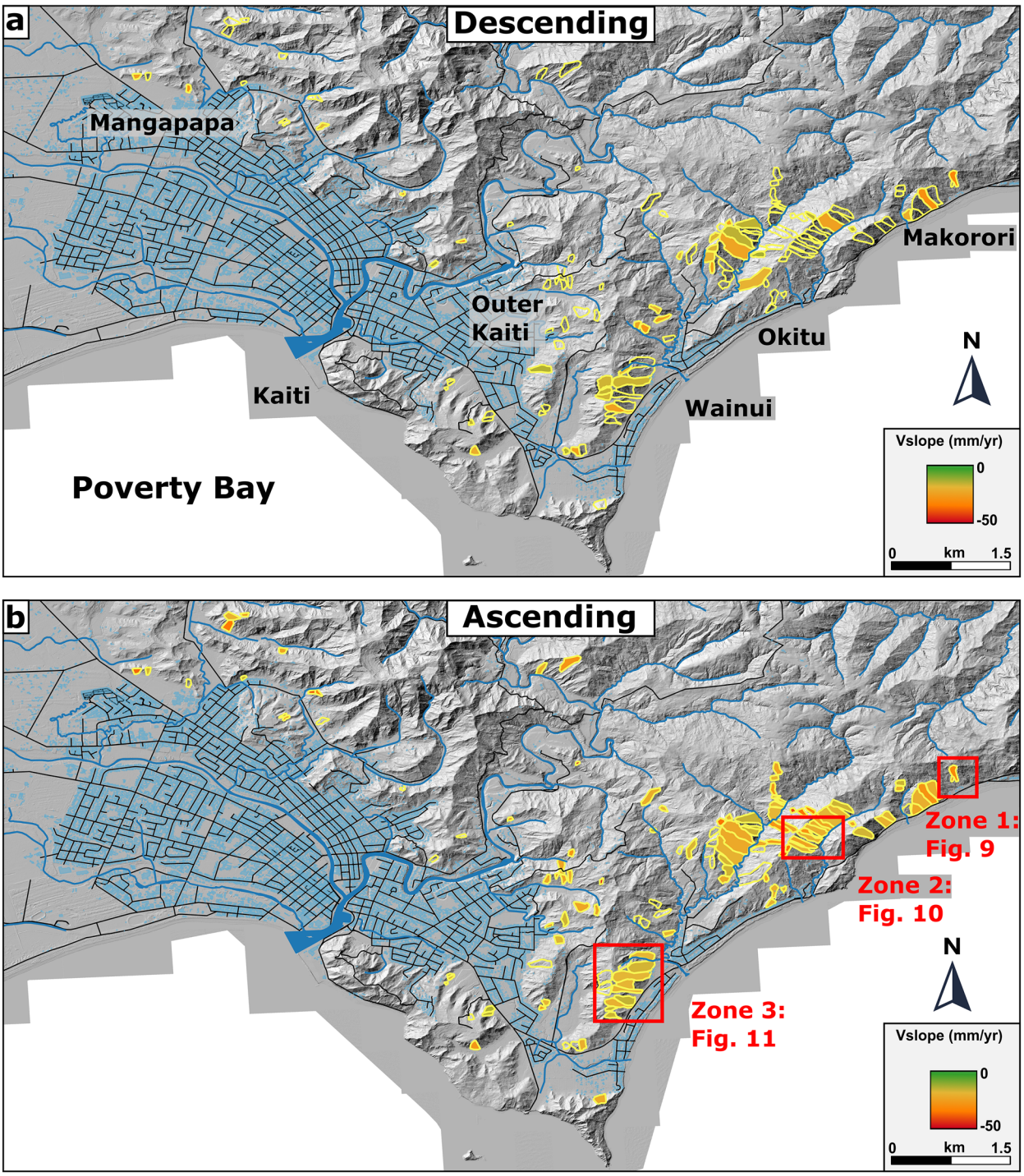

Fig. 8 **a** Map of the unstable slopes identified using the results from the V_{SLOPE} analysis from the descending orbit track. Polygon values represent the average V_{SLOPE} of all the points within the polygon. Negative values (red) indicate movement downslope, and positive values, representing movement uphill, have been removed; **b** unstable slopes identified from the ascending data set

Although InSAR is an effective instrument for landslide detection and analysis (Colesanti and Wasowski 2006; Solari et al. 2020; Rosi et al. 2017), it also presents some well-known limitations which can lead to the underestimation of the actual number of active or dormant landslides in an area (e.g. Bayer et al. 2018). These include: (1) the low density of coherent targets acquired over highly vegetated areas (e.g. Li et al. 2022); (2) the low sensitivity to slope movements that are perpendicular to the satellite LOS (e.g. Colesanti and Wasowski 2006; Notti et al. 2014); (3) excessively rapid movement such as earthflows and small-scale landslides can lead to complete coherence loss, and these can be challenging to detect depending on the satellite's spatial and temporal resolution (Bayer et al. 2018; Rosi

Table 2 V_{SLOPE}, slope and aspect values of the unstable slopes in Fig. 8 for each data set

Orbit geometry	No. of polygons	Min V_{SLOPE} (mm/yr)	Max V_{SLOPE} (mm/yr)	Average V_{SLOPE} (mm/yr)	Average aspect (°)	Average slope (°)
Descending	38	−63.5	−10	−19	200	23
Ascending	106	−75.4	−10	−20	151	23

et al. 2017; Zhou et al. 2020). Indeed, in Gisborne, inconsistencies were observed between potential landslide boundaries delineated in the LiDAR hillshade, aerial imagery and the InSAR deformation patterns, principally due to the difference in the spatial resolution of the data sets. Often, the slopes were grouped into larger failure complexes based on the morphology of the slope and because the resolution of the InSAR data set is unsuitable for mapping such small failures individually. Thus, ideally, these landslide complexes could be subdivided into more discrete slope failures, based on detailed field investigation. For this data set, the pixel size is approximately 15 × 15 m, and if a landslide occupies a small number of pixels, it can be indistinguishable from localized background noise (Xu et al. 2021). Also, several known slope failures within Gisborne city related to retaining wall collapse were not detected, owing to their relatively small spatial extent. In order to increase the number of landslides detected in the urban area, the use of X-band SAR data such as TerraSAR-X would be suitable, which is more sensitive to ground deformation and has a higher spatial resolution than Sentinel-1

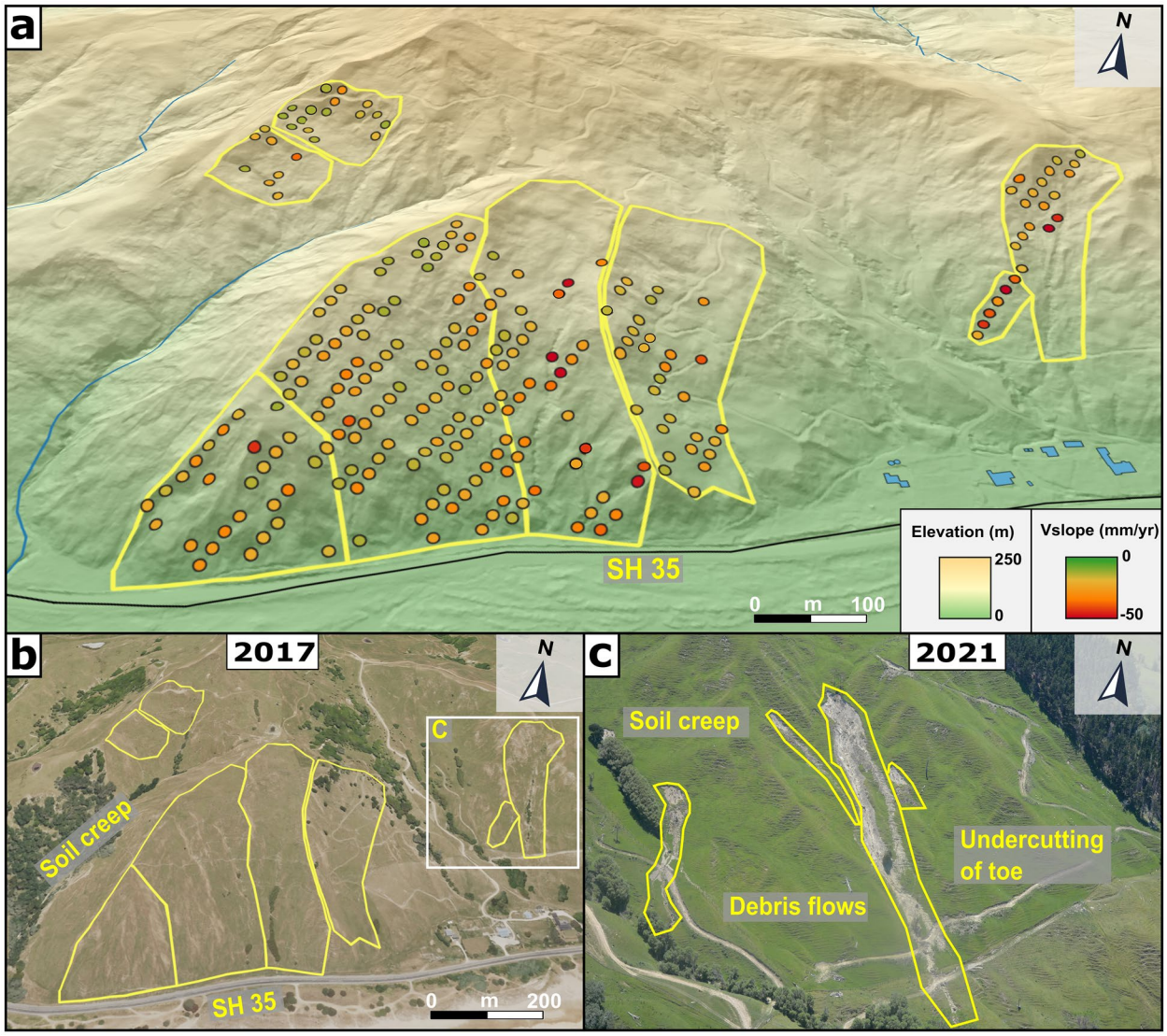

Fig. 9 **a** Map showing the unstable slopes identified in zone 1 with the V_{SLOPE} values. Negative values (red) indicate movement downslope, and positive values, which represent movement uphill, have been removed; **b** high-resolution aerial imagery from 2017 showing exposed sediment along the slopes in zone 1; (**c**) slumping and earthflows on the slope following the November 2021 storm

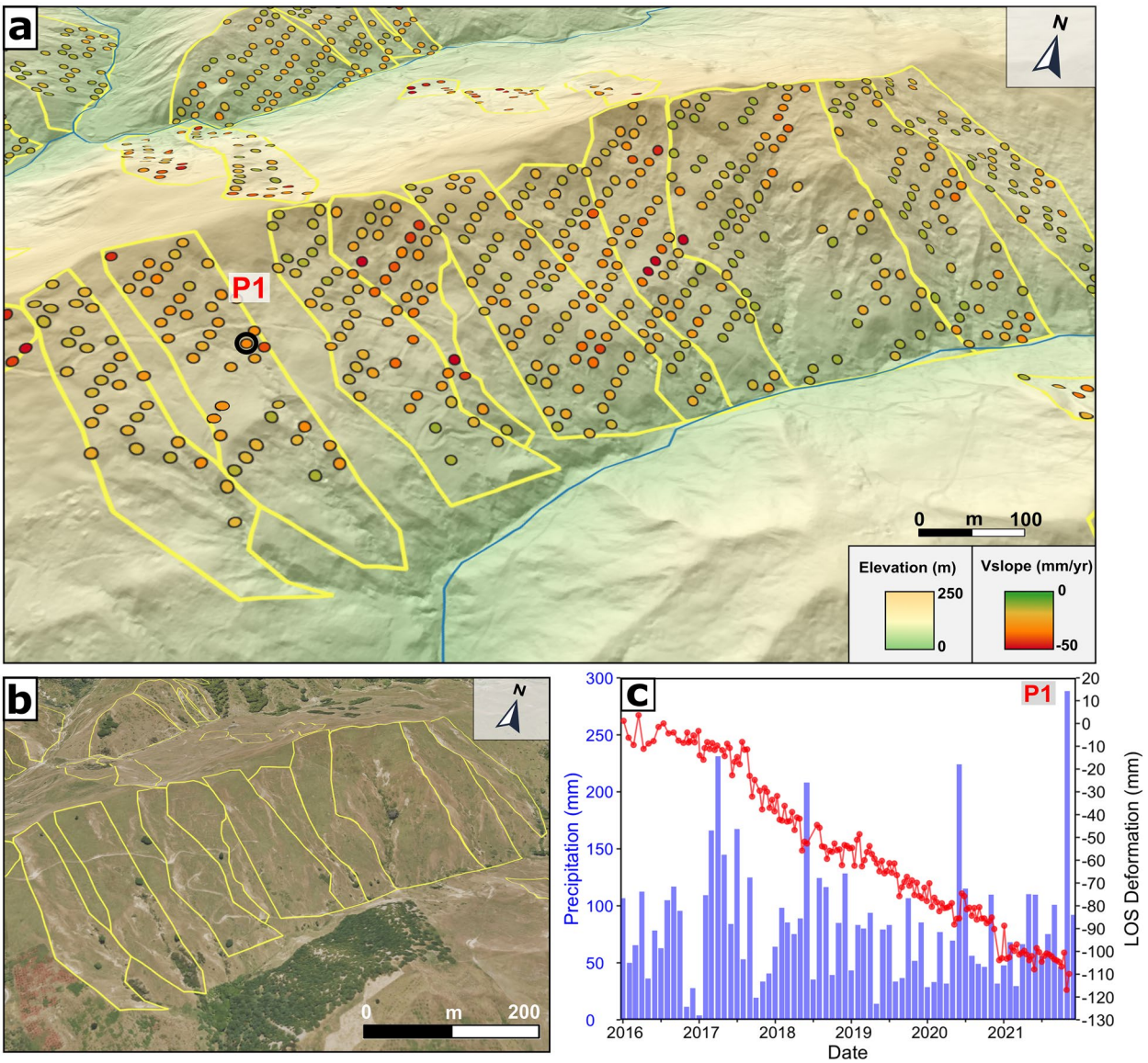

Fig. 10 **a** Map showing the unstable slopes identified in zone 2 with the V_{SLOPE} values. Negative values (red) indicate movement downslope, and positive values, which represent movement uphill, have been removed; **b** high-resolution aerial imagery from 2017 showing exposed sediment along the slopes in zone 2 and undercutting of the slopes by a 4×4 farm track and stream; **c** deformation time series in the direction of the line of sight from point 1 (P1) highlighted in (**a**)

C-band imagery and can provide a higher number of coherent points (Colesanti and Wasowski 2006; Crosetto et al. 2018; Xu et al. 2021). In comparison, the more densely-vegetated areas would benefit from L-band data, which offers greater penetration through vegetation cover due to its longer wavelength, and thus can provide less noisy interferograms in those areas (Colesanti and Wasowski 2006; Xu et al. 2021; Zhao et al. 2012).

Detecting acceleration prior to failure

The linear deformation characteristic of the time series points P1 (Fig. 10c) and P2 (Fig. 11c) indicate that the slopes undergo a constant steady rate of deformation downslope. However, periods of high acceleration appear more clearly related to rainfall input during the wet seasons in autumn and spring (Fig. 12). The steeply-dipping slopes between Okitu and Makorori display higher velocity rates, which reach approximately 120 mm/year during the observation period (Fig. 10c). Indeed, several conditioning factors can accelerate the rate of instability, such as deforestation (e.g. Glade 2003; Page et al. 2000), which reduces the shear strength of the soils, unregulated undercutting of slopes, and debuttressing of the slope toe by streams, which increases the shear stress (Crozier 2010; Glade 2003; Lacroix et al. 2020; Page et al. 2000). In particular, as elsewhere in New Zealand (e.g. Palma et al. 2020), the prolonged heavy rainfall of ex-tropical cyclones Debbie and Cook in April 2017 increased the pore water pressure, which accelerated slope deformation (Fig. 10c)

causing a loss of coherence within the clays and reducing the shear strength. The high sensitivity of InSAR for detecting slow deformation on slopes aids identification of areas undergoing active deformation, which might otherwise be unnoticeable unless a detailed site investigation is undertaken (Petley et al. 2002). The early detection of precursory displacement is critical before landslides cause damage to buildings and infrastructure (Crosetto et al. 2018). Indeed, in Fig. 9, the V_{SLOPE} values show areas of deformation of up to 75 mm/year, above a gully where an earthflow occurred following the November 2021 heavy rainfall event. These precursory movements on slopes above SH35 were detected with InSAR, and other areas of deformation are highlighted in Fig. 9 above the road. Such slopes have the potential to transition into earthflows or mudflows during heavy rainfall events. The continuous linear deformation trends and identification of precursory slope movements by InSAR are similar to other published studies (e.g. Dong et al. 2017; Handwerger et al. 2019; Moretto et al. 2021). In particular, the study by Dong et al. (2017) on the Xinmo landslide using Sentinel-1 data showed an acceleration of surface displacement, similar to P1 in Fig. 10, which showed continuous deformation and then a sudden acceleration following the November 2021 rainfall event.

Seasonal patterns of deformation

Slow-moving landslides are found worldwide in various geological settings, although they typically occur in weak, clay-rich soil or rock (Lacroix et al. 2020). They can cause substantial damage to

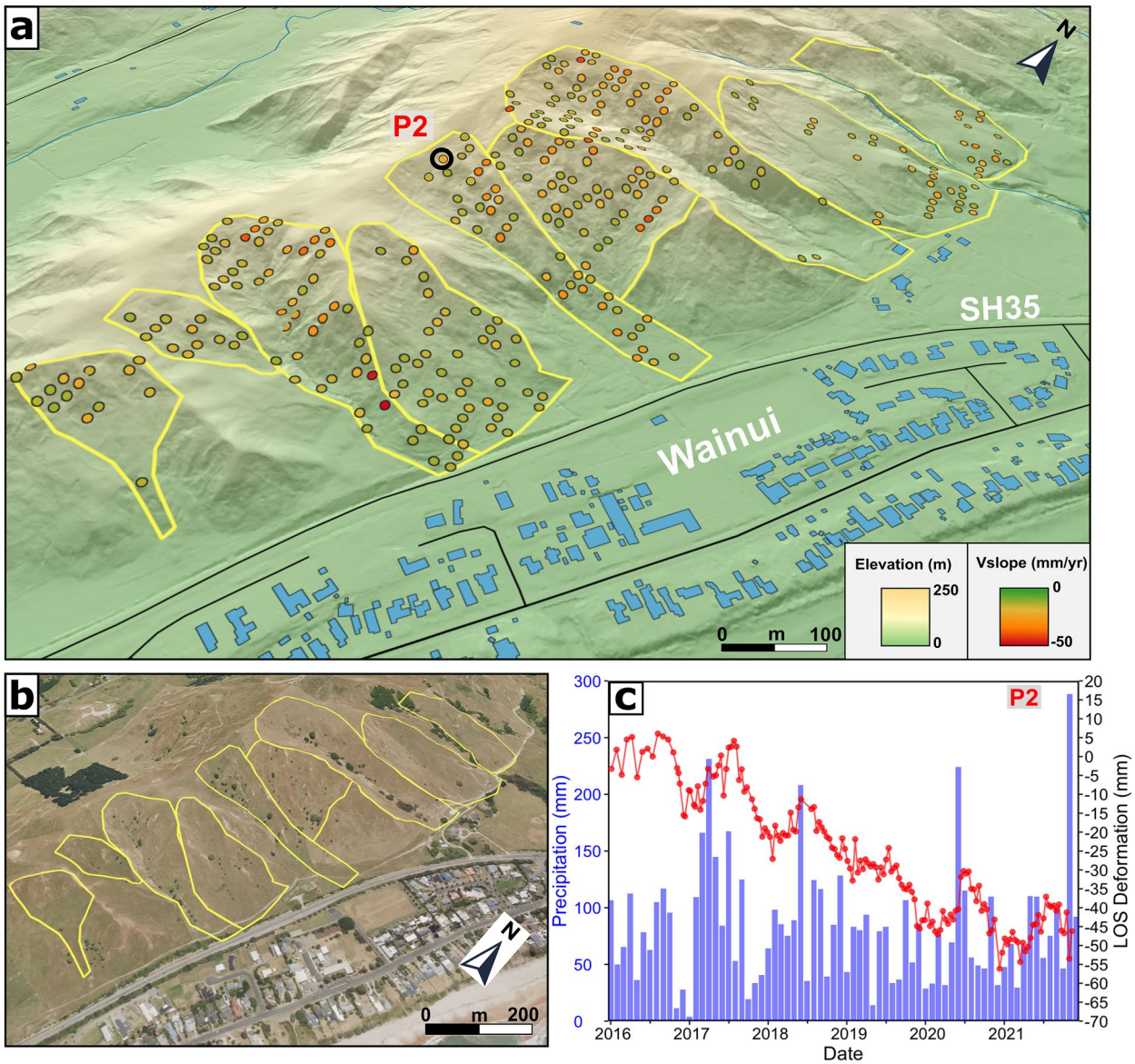

Fig. 11 **a** Map showing the unstable slopes identified in zone 3 with the V_{SLOPE} values. Negative values (red) indicate movement downslope, and positive values, which represent movement uphill, have been removed; **b** high-resolution aerial imagery from 2017 showing exposed sediment along the slopes in zone 3 and the relation of the slopes to SH35 and residential buildings; **c** deformation time series in the direction of the line of sight from point 2 (P2) highlighted in (**a**)

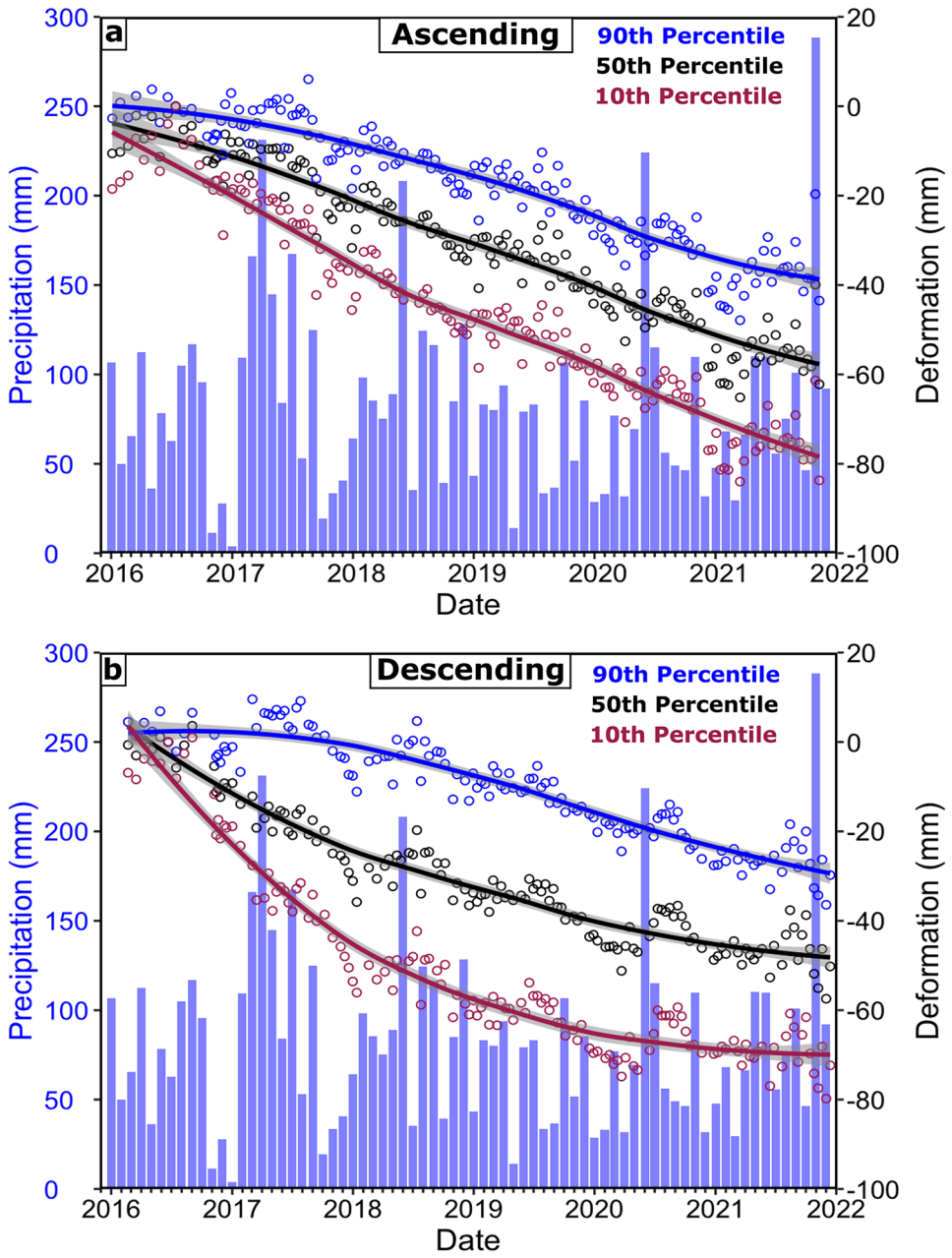

Fig. 12 **a** Time series of the 90th, 50th and 10th percentile of all the coherent points used to identify unstable terrain in Fig. 8b from the ascending data set and; **b** descending data set from Fig. 8a

infrastructure and agriculture and contribute to hillslope erosion and topographic relief (Hilley et al. 2004; Glastonbury and Fell 2008; Mansour et al. 2010; Handwerger et al. 2013; Lacroix et al. 2020). Aside from the impacts of slow, continuous movement, slow-moving landslides can also transition into high-velocity landslides such as earthflows and mudflows (Lacroix et al. 2020). Slow-moving landslides frequently occur in areas of high precipitation and exhibit a seasonal pattern to their deformation (Bayer et al. 2018; Handwerger et al. 2013, 2015; Hilley et al. 2004; Lacroix et al. 2020; Xu et al. 2021). Phases of quiescence and deceleration usually occur during dry periods, which cause cracking and shrinkage within the clay soils and produce preferential flow paths for water to infiltrate (Lacroix et al. 2020). Then, during periods of heavy rainfall, the deformation accelerates due to increases in pore water pressure, which results in a loss of cohesion and reduces the material's shear strength (Glastonbury and Fell 200). Prolonged acceleration and deceleration periods can compromise the large-scale stability of a slope and lead to a catastrophic failure without warning (Federico et al. 2011; Handwerger et al. 2013).

In this study, the InSAR analysis detected continuous slow-moving deformation in shallow soils (Fig. 10c) and cyclic, seasonal displacements (Figs. 11c and 12). In the Gisborne region, the coherence of the interferograms is higher during the winter months than in the summer (Fig. 3). Seasonal change in the coherence of interferograms has been linked to changes in the soil moisture content, and the shrinking and swelling of clays (Rabus et al. 2010; Scott et al. 2017). Drier soils allow the signal from the sensor to penetrate deeper into the soils, causing a more significant backscatter signal than in soils with higher moisture contents (Scott

et al. 2017). A strong seasonal component is observed in the InSAR deformation time series in Fig. 12. The 90th, 50th and 10th percentile of the deformation for the coherent points used to identify the unstable slopes in Fig. 8 are plotted against the average monthly rainfall. The results show that precipitation peaks correlate with deformation peaks (Fig. 12). The seasonal deformation observed is likely related to the shrink-swell movement of the smectite and bentonite-rich soils in the Gisborne region (Cook et al. 2022). Following months of heavy rainfall, deformation is observed to move towards the sensor (i.e. upwards), suggesting the clays are swelling due to increased pore water pressure, while in drier summer months, the deformation moves away from the sensor as the clays shrink due to a decrease in the pore water pressure and cause cracking (Fig. 12). The deformation rates between seasons are approximately 10–20 mm/year (Fig. 12). These variations are consistent with the 9 mm/year seasonal change in the Auckland expansive soils, as detected by Ge et al. (2019) using InSAR and the 20 mm/year cyclic displacements measured by Massey et al. (2013) using GPS stations on the Utiku landslide in central North Island, New Zealand. Massey et al. (2013) also observed that seasonal cyclic deformation was synchronous with changes in pore water pressure in similarly soft, Neogene materials to Gisborne (Fig. 12). The response of the ground to the shrink-swell displacements are likely associated with the vertical and horizontal displacements detected on the slopes observed in Fig. 7. The seasonal component is more apparent in the descending data set than in the ascending data and is likely attributable to the higher number of coherent points and higher velocity values observed in the ascending data set (similarly observed by Van Natijne et al. 2022). Although, reaction to significant rainfall events occurs in both data sets (Fig. 12).

In addition to the observed seasonal signal, many of the landslides are located close to the source region of repeating Slow Slip Events (SSEs), which occur along the subduction interface just offshore of Gisborne (e.g. Wallace and Eberhart-Phillips 2013). These transient slip episodes typically have centimetre scale displacements over broad regions and last for periods of weeks. During the observation period, at least 7 SSEs affected the study area. Because the InSAR displacements are relative to points within Gisborne, the magnitude of any SSE signal is likely to be small. To investigate any potential transient signal being incorporated into our landslide time series, we convert the east, north and vertical displacements of a nearby continuous GNSS station (MAKO) into the satellite LOS (Fig. 13). To put them in a consistent reference frame with the InSAR, these are made relative to another local GNSS station (GISB) which is located ~ 10 km west of Gisborne. In a final step, we detrend the LOS displacements shown in Fig. 12 and compare them with the expected signal caused by the SSEs. While only a small component of the total signal, most of the SSEs are accompanied by a subtle change in the displacement time series from the landslides. Although the SSEs have equivalent seismic moments of Mw 6 + events, due to their slow nature with slip occurring over many weeks, it is unlikely that they have any influence on the landslides themselves.

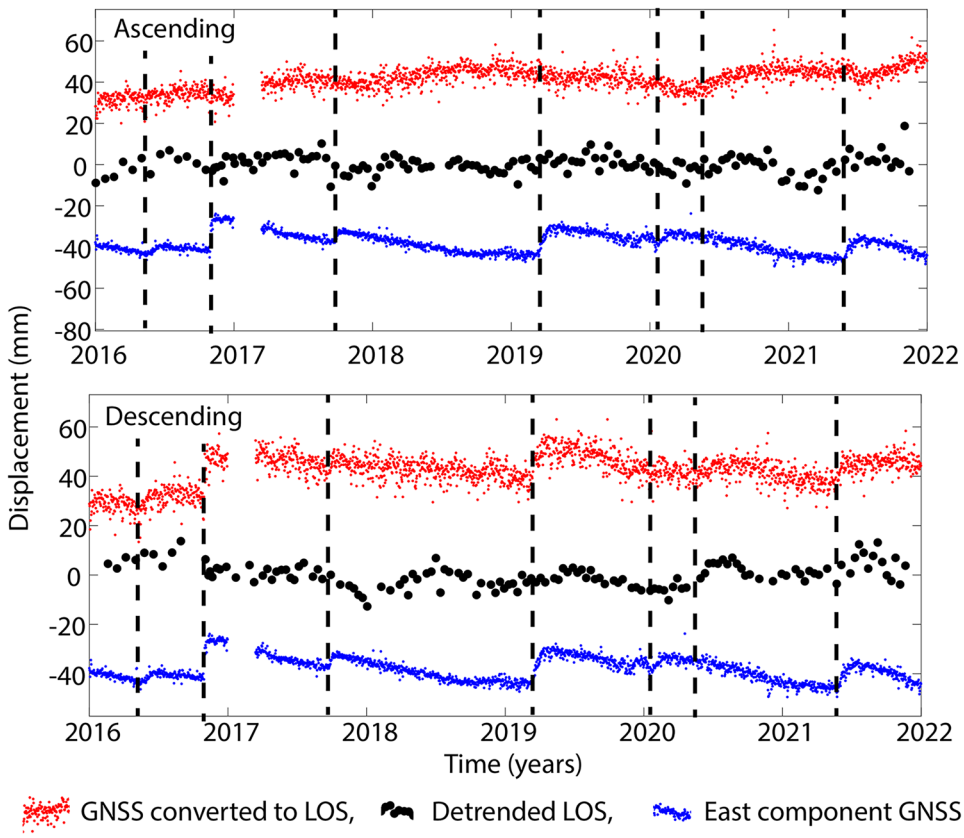

Fig. 13 Comparison between detrended InSAR time series of the average landslide displacements for ascending and descending data with the GNSS time series at MAKO relative to GISB. The red dots show the 3 components of the GNSS converted into the satellite LOS direction. The black dots are the detrended InSAR time series from Fig. 12, and the blue dots show the east component of the GNSS. The dashed lines show the timings of SSE events

Conclusions

This study focused on slow-moving shallow soil landslides driven by soil creep and the shrink-swell of clays, which in Gisborne often transition into fast-moving earth and mudflows during heavy rainfall events. The InSAR analysis has shown a high consistency between areas of deformation and shallow soil failures observed in the aerial imagery and the field, allowing an updated inventory of Gisborne's landslides, which previously only consisted of point locations. The InSAR data set was used to identify previously unknown unstable slopes and provided a back analysis of unstable areas to determine the movement rates over time and correlate periods of accelerations with potential triggering factors. In total, 132 areas of deformation were identified using the InSAR results, LiDAR hillshade, aerial imagery and site photos. Unstable slopes are primarily associated with steep slopes affected by deforestation, overgrazing and undercut by roads, rivers and farm tracks. Velocities increased rapidly, specifically, following ex-tropical cyclones in April 2017, and more generally following heavy rainfall events during winter months. Maximum velocities of 79 mm/year in the V_{SLOPE} direction were detected. Seasonal displacements due to shrinking and swelling of expansive soils are also detectable, and these are synchronous with wet and dry periods, ranging from 10 to 20 mm/year between winter and summer. In Gisborne, the slow-moving soil creep and shrink-swell related displacements cause a continuous motion of the soil's downslope. During heavy rainfall events, the pore water pressure increases and slumps transition into fast-moving earth or mudflows, which often mobilise down channels and gullies. Thus, detecting precursory deformation areas before transition into fast-moving flows or slides is crucial for landslide risk planning (Crosetto et al. 2018). The satellite-based InSAR analysis in this study has proved to be a suitable tool to update existing landslide inventories and pinpoint zones of deformation. These locations can be targeted with more detailed geotechnical site investigation and monitoring instrumentation such as extensometers, inclinometers, piezometers and GPS. Taken together, this will assist with future policy and risk decision-making in anticipation of future landslide activity across the Gisborne region.

Acknowledgements

Gisborne District Council is thanked for provision of the LiDAR data and aerial imagery, Andrea Wolter at GNS for providing several site photos, and the National Institute of Water and Atmospheric Research (NIWA) provided climate station data via their Cliflo database.

Funding

Open Access funding enabled and organized by CAUL and its Member Institutions. This research is funded by the Earthquake Commission (EQC) via grant numbers 18/U770 and 1965/20799, which funded Matthew Cook's PhD scholarship.

Data availability

The data that support the findings of this study are available from the Gisborne District Council but restrictions apply to the availability of these data, which were used under licence for the current study, and so are not publicly available. Data are however available from the authors upon reasonable request and with permission of the Gisborne District Council.

Declarations

Competing interests The authors declare no competing interests.

References

Aslan G, Foumelis M, Raucoules D, de Michele M, Bernardie S, Cakir Z (2020) Landslide mapping and monitoring using persistent scatterer interferometry (PSI) technique in the French Alps. Remote Sens 12(8):1305. https://doi.org/10.3390/rs12081305

Atzori S, Tolomei C, Antonioli A, Merryman Boncori JP, Bannister S, Trasatti E, Pasquali P, Salvi S (2012) The 2010–2011 Canterbury, New Zealand, seismic sequence: multiple source analysis from InSAR data and modeling. J of Geophys Res: Solid Earth 117(B8). https://doi.org/10.1029/2012jb009178

Barnhart WD, Willis MJ, Lohman RB, Melkonian AK (2011) InSAR and optical constraints on fault slip during the 2010–2011 New Zealand earthquake sequence. Seismol Res Lett 82(6):815–823. https://doi.org/10.1785/gssrl.82.6.815

Barra A, Monserrat O, Mazzanti P, Esposito C, Crosetto M, Scarascia Mugnozza G (2016) First insights on the potential of Sentinel-1 for landslides detection. Geomat, Nat Hazards and Risk 7(6):1874–1883. https://doi.org/10.1080/19475705.2016.1171258

Basher LR (2013) Erosion processes and their control in New Zealand. In: Dymond JR (ed) Ecosystem services in New Zealand – conditions and trends. Manaaki Whenua Press, Lincoln, New Zealand, pp 363–374. https://doi.org/10.7931/DL1MS3

Bayer B, Simoni A, Mulas M, Corsini A, Schmidt D (2018) Deformation responses of slow moving landslides to seasonal rainfall in the Northern Apennines, measured by InSAR. Geomorphol 308:293–306. https://doi.org/10.1016/j.geomorph.2018.02.020

Béjar-Pizarro M, Notti D, Mateos RM, Ezquerro P, Centolanza G, Herrera G, Bru G, Sanabria M, Solari L, Duro J, Fernández J (2017) Mapping vulnerable urban areas affected by slow-moving landslides using Sentinel-1 InSAR data. Remote Sens 9(9):876. https://doi.org/10.3390/rs9090876

Beetham, RD, Grant H (2006) Reconnaissance of landslide and flood damage in the Gisborne area caused by the 2005 Labour Weekend storm. Inst Geol Nucl Sci Rep 2006/022 35 p

Berardino P, Fornaro G, Lanari R, Sansosti E (2002) A new algorithm for surface deformation monitoring based on small baseline differential SAR interferograms. IEEE Transactions on Geoscience and Remote Sens 40(11):2375–2383. https://doi.org/10.1109/tgrs.2002.803792

Bianchini S, Herrera G, Mateos R, Notti D, Garcia I, Mora O, Moretti S (2013) Landslide activity maps generation by means of persistent scatterer interferometry. Remote Sens 5(12):6198–6222. https://doi.org/10.3390/rs5126198

Colesanti C, Wasowski J (2006) Investigating landslides with space-borne Synthetic Aperture Radar (SAR) interferometry. Eng Geol 88(3–4):173–199. https://doi.org/10.1016/j.enggeo.2006.09.013
Cook ME, Brook MS, Tunnicliffe J, Cave M, Gulick NP (2022) Preliminary investigation of emerging suburban landsliding in Gisborne, New Zealand. Q J of Eng Geol and Hydrogeol qjegh2021–087. https://doi.org/10.1144/qjegh2021-087
Crosetto M, Copons R, Cuevas-González M, Devanthéry N, Monserrat O (2018) Monitoring soil creep landsliding in an urban area using persistent scatterer interferometry (El Papiol, Catalonia, Spain). Landslides 15(7):1317–1329. https://doi.org/10.1007/s10346-018-0965-5
Crozier M (2010) Landslide geomorphology: An argument for recognition, with examples from New Zealand. Geomorphol 120(1–2):3–15. https://doi.org/10.1016/j.geomorph.2009.09.010
Crozier MJ (2005) Multiple-occurrence regional landslide events in New Zealand: Hazard management issues. Landslides 2(4):247–256. https://doi.org/10.1007/s10346-005-0019-7
Cruden DM (1990) Landslides: extent and economic significance. Can Geotec J 27(3):408. https://doi.org/10.1139/t90-056
Davies N, Cave M (2017) Slope Instability Wallis Road. Initial Technical Report. Gisborne, New Zealand.
De Luca C, Casu F, Manunta M, Onorato G, Lanari R (2022) Comments on "Study of Systematic Bias in Measuring Surface Deformation With SAR Interferometry." IEEE Trans on Geosci and Remote Sens 60:1–5. https://doi.org/10.1109/tgrs.2021.3103037
Del Soldato M, Solari L, Poggi F, Raspini F, Tomás R, Fanti R, Casagli N (2019) Landslide-Induced Damage Probability Estimation Coupling InSAR and Field Survey Data by Fragility Curves. Remote Sens 11(12):1486. https://doi.org/10.3390/rs11121486
Dong J, Zhang L, Li M, Yu Y, Liao M, Gong J, Luo H (2017) Measuring precursory movements of the recent Xinmo landslide in Mao County, China with Sentinel-1 and ALOS-2 PALSAR-2 datasets. Landslides 15(1):135–144. https://doi.org/10.1007/s10346-017-0914-8
Elliott JR, Nissen EK, England PC, Jackson JA, Lamb S, Li Z, Oehlers M, Parsons B (2012) Slip in the 2010–2011 Canterbury earthquakes, New Zealand. J of Geophys Res: Solid Earth 117(B3). https://doi.org/10.1029/2011jb008868
Federico A, Popescu M, Elia G, Fidelibus C, Internò G, Murianni A (2011) Prediction of time to slope failure: a general framework. Environ Earth Sci 66(1):245–256. https://doi.org/10.1007/s12665-011-1231-5
Ferretti A (2014) Satellite InSAR Data: Reservoir Monitoring from Space (EET 9) (1st ed.). EAGE. https://doi.org/10.1109/MGRS.2015.2398392
Ferretti A, Fumagalli A, Novali F, Prati C, Rocca F, Rucci A (2011) A new algorithm for processing interferometric data-stacks: SqueeSAR. IEEE Transactions on Geoscience and Remote Sens 49(9):3460–3470. https://doi.org/10.1109/TGRS.2011.2124465
Ferretti A, Prati C, Rocca F (2001) Permanent scatterers in SAR interferometry. IEEE Transactions on Geosci and Remote Sens 39(1):8–20
Franks CAM (1988) Engineering Geological Assessment of the impact of Cyclone Bola March 1988 on the damline & dam extension line sections of the Gisborne City water supply. EG88/011
Ge L, Du Z, Khalili N (2019) Assessing expansive soil risk using remote sensing. Int Soc Soil Mech Geotech Eng
Glade T (1998) Establishing the frequency and magnitude of landslide-triggering rainstorm events in New Zealand. Environ Geol 35(2–3):160–174. https://doi.org/10.1007/s002540050302
Glade T (2003) Landslide occurrence as a response to land use change: a review of evidence from New Zealand. CATENA 51(3–4):297–314. https://doi.org/10.1016/s0341-8162(02)00170-4
Glastonbury J, Fell R (2008) Geotechnical characteristics of large slow, very slow, and extremely slow landslides. Can Geotec J 45(7):984–1005. https://doi.org/10.1139/t08-021
Handwerger AL, Huang MH, Fielding EJ, Booth AM, Bürgmann, R (2019) A shift from drought to extreme rainfall drives a stable landslide to catastrophic failure. Sci Rep 9(1). https://doi.org/10.1038/s41598-018-38300-0
Handwerger AL, Roering JJ, Schmidt DA (2013) Controls on the seasonal deformation of slow-moving landslides. Earth and Planet Sci Lett 377–378:239–247. https://doi.org/10.1016/j.epsl.2013.06.047
Handwerger AL, Roering JJ, Schmidt DA, Rempel AW (2015) Kinematics of earthflows in the Northern California Coast Ranges using satellite interferometry. Geomorphol 246:321–333. https://doi.org/10.1016/j.geomorph.2015.06.003
Hamling IJ (2020) InSAR observations over the Taupō Volcanic Zone's cone volcanoes: insights and challenges from the New Zealand volcano supersite. N.Z. J of Geol and Geophys 1–11. https://doi.org/10.1080/00288306.2020.1721545
Hamling IJ, Hreinsdóttir S, Fournier N (2015) The ups and downs of the TVZ: Geodetic observations of deformation around the Taupo Volcanic Zone, New Zealand. J of Geophys Res: Solid Earth 120(6):4667–4679. https://doi.org/10.1002/2015jb012125
Harvey M (2021) Sentinel-1 InSAR captures 2019 catastrophic White Island eruption. J of Volcanol and Geotherm Res 411:107124. https://doi.org/10.1016/j.jvolgeores.2020.107124
Hilley GE, BüRgmann R, Ferretti A, Novali F, Rocca F (2004) Dynamics of Slow-Moving Landslides from Permanent Scatterer Analysis. Sci 304(5679):1952–1955. https://doi.org/10.1126/science.1098821
Hole J, Bromley C, Stevens N, Wadge G (2007) Subsidence in the geothermal fields of the Taupo Volcanic Zone, New Zealand from 1996 to 2005 measured by InSAR. J of Volcanol and Geotherm Res 166(3–4):125–146. https://doi.org/10.1016/j.jvolgeores.2007.07.013
Hooper A (2008) A multi-temporal InSAR method incorporating both persistent scatterer and small baseline approaches. Geophys Res Lett 35(16). https://doi.org/10.1029/2008GL034654
Hu J, Li ZW, Ding XL, Zhu JJ, Zhang L, Sun Q (2012) 3D coseismic Displacement of 2010 Darfield, New Zealand earthquake estimated from multi-aperture InSAR and D-InSAR measurements. J of Geodesy 86(11):1029–1041. https://doi.org/10.1007/s00190-012-0563-6
Hu J, Li Z, Ding X, Zhu J, Zhang L, Sun Q (2014) Resolving three-dimensional surface displacements from InSAR measurements: A review. Earth Sci Rev 133:1–17. https://doi.org/10.1016/j.earscirev.2014.02.005
Hungr O, Leroueil S, Picarelli L (2014) The Varnes classification of landslide types, an update. Landslides 11(2):167–194. https://doi.org/10.1007/s10346-013-0436-y
Isya NH, Niemeier W, Gerke M (2019) 3D Estimation of slow ground motion using InSAR and the slope aspect assumption, a case study: The Puncak Pass landslide, Indonesia. ISPRS Annals of Photogrammetry, Remote Sens & Spat Infor Sci IV-2/W5:623–630. https://doi.org/10.5194/isprs-annals-iv-2-w5-623-2019
Kromer RA, Hutchinson DJ, Lato MJ, Gauthier D, Edwards T (2015) Identifying rock slope failure precursors using LiDAR for transportation corridor hazard management. Eng Geol 195:93–103. https://doi.org/10.1016/j.enggeo.2015.05.012
Lacoste A, Loncke L, Chanier F, Bailleul J, Vendeville BC, Mahieux G (2009) Morphology and structure of a landslide complex in an active margin setting: The Waitawhiti complex, North Island. New Zealand Geomorphol 109(3–4):184–196. https://doi.org/10.1016/j.geomorph.2009.03.001
Lacroix P, Handwerger AL, Bièvre G (2020) Life and death of slow-moving landslides. Nat Rev Earth & Environ 8:404–419. https://doi.org/10.1038/s43017-020-0072-8
Lanari R, Lundgren P, Manzo M, Casu F (2004) Satellite radar interferometry time series analysis of surface deformation for Los Angeles, California. Geophysical Res Lett 31(23). https://doi.org/10.1029/2004GL021294
Liu J, Zhang G, Wang J, Sun G, Zhang Y, Wang Y, Qu C, Shan X (2022) Three-dimensional coseismic deformation of the 2016 MW7.8 Kaikuora, New Zealand earthquake obtained by InSAR and offsets measurements. Geodesy and Geodyn. https://doi.org/10.1016/j.geog.2022.02.004
Li S, Xu W, Li Z (2022) Review of the SBAS InSAR Time-series algorithms, applications, and challenges. Geodesy and Geody 13(2):114–126. https://doi.org/10.1016/j.geog.2021.09.007
Mansour MF, Morgenstern NR, Martin CD (2010) Expected damage from displacement of slow-moving slides. Landslides 8(1):117–131. https://doi.org/10.1007/s10346-010-0227-7
Massey C, Petley D, McSaveney M (2013) Patterns of movement in reactivated landslides. Eng Geol 159:1–19. https://doi.org/10.1016/j.enggeo.2013.03.011

Mazengarb C (1997) Slope instability and mud volcano hazard assessment, Gisborne District Council. Institute of Geological & Nuclear Sciences client report. 44692d. 13A
Moretto S, Bozzano F, Mazzanti P (2021) The Role of Satellite InSAR for Landslide Forecasting: Limitations and Openings. Remote Sens 13(18):3735. https://doi.org/10.3390/rs13183735
Notti D, Herrera G, Bianchini S, Meisina C, García-Davalillo JC, Zucca F (2014) A methodology for improving landslide PSI data analysis. Int J of Remote Sens 35(6):2186–2214. https://doi.org/10.1080/01431161.2014.889864
Osmanoğlu B, Sunar F, Wdowinski S, Cabral-Cano E (2016) Time series analysis of InSAR data: Methods and trends. ISPRS J of Photogrammetry and Remote Sens 115:90–102. https://doi.org/10.1016/j.isprsjprs.2015.10.003
Page M, Trust rum N, Gomez B (2000) Implications of a Century of Anthropogenic Erosion for Future Land Use in the Gisborne-East Coast Region of New Zealand. N.Z. Geogr 56(2):13–24. https://doi.org/10.1111/j.1745-7939.2000.tb01571.x
Palma A, Garrill R, Brook MS, Richards N, Tunnicliffe J (2020) Reactivation of coastal landsliding at Sunkist Bay, Auckland, following ex-Tropical Cyclone Debbie, 5 April 2017. Landslides 17(11):2659–2669. https://doi.org/10.1007/s10346-020-01474-8
Petley DN, Bulmer MH, Murphy W (2002) Patterns of movement in rotational and translational landslides. Geol 30(8):719. https://doi.org/10.1130/0091-7613(2002)030%3c0719:POMIRA%3e2.0.CO;2
Phillips C, Marden M, Basher LR (2018) Geomorphology and forest management in New Zealand's erodible steeplands: An overview. Geomorphol 307:107–121. https://doi.org/10.1016/j.geomorph.2017.07.031
Rabus B, Wehn H, Nolan M (2010) The Importance of Soil Moisture and Soil Structure for InSAR Phase and Backscatter, as Determined by FDTD Modeling. IEEE Trans on Geosci and Remote Sens 48(5):2421–2429. https://doi.org/10.1109/tgrs.2009.2039353
Rosen PA, Gurrola E, Sacco GF, Zebker H (2012) The InSAR scientific computing environment. In EUSAR 2012; 9th European Conference on Synthetic Aperture Radar 730–733
Rosi A, Tofani V, Tanteri L, Tacconi Stefanelli C, Agostini A, Catani F, Casagli N (2017) The new landslide inventory of Tuscany (Italy) updated with PS-InSAR: geomorphological features and landslide distribution. Landslides 15(1):5–19. https://doi.org/10.1007/s10346-017-0861-4
Schlögel R, Doubre C, Malet JP, Masson F (2015) Landslide deformation monitoring with ALOS/PALSAR imagery: A D-InSAR geomorphological interpretation method. Geomorphol 231:314–330. https://doi.org/10.1016/j.geomorph.2014.11.031
Scott CP, Lohman RB, Jordan TE (2017) InSAR constraints on soil moisture evolution after the March 2015 extreme precipitation event in Chile. Sci Rep 7(1). https://doi.org/10.1038/s41598-017-05123-4
Simons M, Rosen PA (2007) Interferometric Synthetic Aperture Radar Geodesy Geodesy 3:391–446. https://doi.org/10.1016/B978-044452748-6.00059-6
Smith HG, Spiekermann R, Betts H, Neverman AJ (2021) Comparing methods of landslide data acquisition and susceptibility modelling: Examples from New Zealand. Geomorphol 381:107660. https://doi.org/10.1016/j.geomorph.2021.107660
Speden I (2004) Geological hazard and risk assessment in the Wheatstone Road – Sponge Bay area, Gisborne City. Inst Geol Nucl Sci Sci Rep 2004/29 9 p
Solari L, del Soldato M, Raspini F, Barra A, Bianchini S, Confuorto P, Casagli N, Crosetto M (2020) Review of Satellite Interferometry for Landslide Detection in Italy. Remote Sens 12(8):1351. https://doi.org/10.3390/rs12081351
Turner AK (2018) Social and environmental impacts of landslides. Innovative Infrastruct Solut 3(1). https://doi.org/10.1007/s41062-018-0175-y
Van Natijne A, Bogaard T, van Leijen F, Hanssen R, Lindenbergh R (2022) World-wide InSAR sensitivity index for landslide deformation tracking. Int J of Appl Earth Obs and Geoinformation 111:102829. https://doi.org/10.1016/j.jag.2022.102829
Vincent P, Clarke V (1980) Terracette morphology and soil properties: A note on a canonical correlation study. Earth Surf Proces 5(3):291–295. https://doi.org/10.1002/esp.3760050307
Wallace LM, Eberhart-Phillips D (2013) Newly observed, deep slow slip events at the central Hikurangi margin, New Zealand: Implications for downdip variability of slow slip and tremor, and relationship to seismic structure. Geophys Res Lett 40(20):5393–5398. https://doi.org/10.1002/2013gl057682
Wasowski J, Bovenga F (2014) Investigating landslides and unstable slopes with satellite Multi Temporal Interferometry: Current issues and future perspectives. Eng Geol 174:103–138. https://doi.org/10.1016/j.enggeo.2014.03.003
Xu Y, Schulz WH, Lu Z, Kim J, Baxstrom K (2021) Geologic controls of slow-moving landslides near the US West Coast. Landslides 18(10):3353–3365. https://doi.org/10.1007/s10346-021-01732-3
Xue C, Chen K, Tang H, Liu P (2021) Heavy rainfall drives slow-moving landslide in Mazhe Village, Enshi to a catastrophic collapse on 21 July 2020. Landslides 19(1):177–186. https://doi.org/10.1007/s10346-021-01782-7
Yunjun Z, Fattahi H, Amelung F (2019) Small baseline InSAR time series analysis: Unwrapping error correction and noise reduction, Computers & Geosci 133:104331. https://doi.org/10.1016/j.cageo.2019.104331
Zhou C, Cao Y, Yin K, Wang Y, Shi X, Catani F, Ahmed B (2020) Landslide Characterization Applying Sentinel-1 Images and InSAR Technique: The Muyubao Landslide in the Three Gorges Reservoir Area. China Remote Sens 12(20):3385. https://doi.org/10.3390/rs12203385
Zhao C, Lu Z, Zhang Q, de la Fuente J (2012) Large-area landslide detection and monitoring with ALOS/PALSAR imagery data over Northern California and Southern Oregon, USA. Remote Sens of Environ 124:348–359. https://doi.org/10.1016/j.rse.2012.05.025

Matthew E. Cook (✉) · **Martin S. Brook** · **Jon F. Tunnicliffe**
School of Environment, The University of Auckland, Auckland 1010, New Zealand
Email: mcoo951@aucklanduni.ac.nz

Ian J. Hamling
GNS Science, Lower Hutt, New Zealand

Murry Cave
Gisborne District Council, Gisborne 4010, New Zealand

Rachel Holley
CGG Satellite Mapping, Crockham Park, Edenbridge TN8 6SR, UK